Monthly Notices
of the
ROYAL ASTRONOMICAL SOCIETY

MNRAS **461,** 560–577 (2016)
Advance Access publication 2016 June 7

doi:10.1093/mnras/stw1338

A multiwavelength photometric census of AGN and star formation activity in the brightest cluster galaxies of X-ray selected clusters

T. S. Green,[1★] A. C. Edge,[1★] J. P. Stott,[1,2] H. Ebeling,[3] W. S. Burgett,[4]
K. C. Chambers,[3] P. W. Draper,[1] N. Metcalfe,[1] N. Kaiser,[3] R. J. Wainscoat[3]
and C. Waters[3]

[1] *Centre for Extragalactic Astronomy, Durham University, South Road, Durham DH1 3LE, UK*
[2] *Sub-department of Astrophysics, Department of Physics, University of Oxford, Denys Wilkinson Building, Keble Road, Oxford OX1 3RH, UK*
[3] *Institute for Astronomy, University of Hawaii, 2680 Woodlawn Drive, Honolulu, HI 96822, USA*
[4] *GMTO Corporation, 465 N. Halstead St, Suite 250, Pasadena, CA 91107, USA*

Accepted 2016 June 2. Received 2016 May 31; in original form 2016 January 29

ABSTRACT

Despite their reputation as being ‘red and dead’, the unique environment inhabited by brightest cluster galaxies (BCGs) can often lead to a self-regulated feedback cycle between radiatively cooling intracluster gas and star formation and active galactic nucleus (AGN) activity in the BCG. However the prevalence of ‘active’ BCGs, and details of the feedback involved, are still uncertain. We have performed an optical, UV and mid-IR photometric analysis of the BCGs in 981 clusters at $0.03 < z < 0.5$, selected from the *ROSAT* All Sky Survey. Using Pan-STARRS PS1 3π, *GALEX* and *WISE* survey data we look for BCGs with photometric colours which deviate from that of the bulk population of passive BCGs – indicative of AGN and/or star formation activity within the BCG. We find that whilst the majority of BCGs are consistent with being passive, at least 14 per cent of our BCGs show a significant colour offset from passivity in at least one colour index. And, where available, supplementary spectroscopy reveals the majority of these particular BCGs show strong optical emission lines. On comparing BCG ‘activity’ with the X-ray luminosity of the host cluster, we find that BCGs showing a colour offset are preferentially found in the more X-ray luminous clusters, indicative of the connection between BCG ‘activity’ and the intracluster medium.

Key words: galaxies: active – galaxies: clusters: general – galaxies: elliptical and lenticular, cD – X-rays: galaxies: clusters.

1 INTRODUCTION

As the most massive galaxies in the Universe, and positioned at the centre of the cluster potential, the evolution of brightest cluster galaxies (BCGs) is affected by the intracluster medium (ICM). In turn, feedback effects from active galactic nuclei (AGN) and star formation activity in the BCG affects the evolution of the ICM. A self-regulated cycle of radiative cooling and AGN heating is widely acknowledged, however, the physics of this heating mechanism are not well understood. With photometric surveys becoming ever larger, identification of active BCG candidates through photometry is crucial in our attempts to understand the important role that feedback plays in galaxy evolution.

Early-type galaxies in the cores of galaxy clusters are typically referred to as ‘red and dead’ galaxies – their stellar populations have been passively evolving since forming in an essentially instantaneous burst of SF at high redshift ($z > 2$) (e.g. Stanford, Eisenhardt & Dickinson 1998; Andreon 2003; Thomas et al. 2005; Mei et al. 2006; van Dokkum & van der Marel 2007). Located at the centre of the cluster potential however, and surrounded by dense intracluster gas, BCGs occupy a unique environment, with an enhanced likelihood to foster cool gas and star formation.

The ICM, which outweighs the constituent galaxies by a factor of 10 in rich clusters (Lin, Mohr & Stanford 2003), exists at typical temperatures of $T \sim 10^{7-8}$ K and, as a result, radiates away huge amounts of energy through thermal Bremsstrahlung X-ray emission ($L_X \sim 10^{43-45}$ erg s^{-1}). Models predict that an unopposed process of such radiative cooling would lead to gas cooling through intermediate temperatures, a reservoir of cold gas in the centre of clusters, and subsequent star formation. However, X-ray observations with *XMM–Newton* and *Chandra* of clusters with very peaked central emission, and hence cooling time-scales shorter than the age of the system – known as ‘cool core’ clusters – reveal that this is not the case. The observed temperatures of the ‘cool cores’ are rarely

---

★ E-mail: t.s.green@durham.ac.uk (TSG); alastair.edge@durham.ac.uk (ACE)

Published by Oxford University Press on behalf of the Royal Astronomical Society

lower than 1/3 of the virial temperature, warmer than pure cooling models would predict, and the mass of cooling gas and the star formation rates are lower than predicted. As the deposition rate of cool gas in such clusters was expected to cause a flow of gas of the order of 100–1000 s $\mathrm{M}_\odot\,\mathrm{yr}^{-1}$ (Fabian 1994), this came to be known as the 'cooling flow' problem. The realization now is that a heating mechanism must exist, offsetting the cooling rate, and that a self regulated cycle of cooling and heating occurs. The primary source of this heating is thought to be AGN feedback (Fabian 2012; McNamara & Nulsen 2012).

The majority of cool core clusters are observed to have a central radio galaxy (Burns 1990; Hogan et al. 2015) and heating via this AGN activity is supported by observations of co-located X-ray cavities and radio lobes around radio bright BCGs (e.g. Boehringer et al. 1993; McNamara et al. 2000; Hlavacek-Larrondo et al. 2015). Cavities, resulting from the displacement of the X-ray emitting ICM by jet driven outflowing plasma, are seen in $\geq$70 per cent of cool core clusters (Dunn & Fabian 2006; Hlavacek-Larrondo et al. 2012). The energy necessary to create these cavities is generally sufficient to balance the energy loss through radiative cooling (Rafferty et al. 2006; McNamara & Nulsen 2007). The exact nature of this heating is however, still disputed with several mechanisms proposed (see Fabian 2012 and McNamara & Nulsen 2012 for reviews). Despite the fact it is common to see radio emission from BCGs, and the evidence suggests that the AGN often play an important role over time-scales of at least 1 Gyr, BCGs which exhibit signs of an on-going strong AGN outburst are rare because of the short AGN duty cycle. Hence, in order to constrain the prevalence of ongoing AGN in BCGs, over a wide range of AGN power, it is necessary to have a large sample of BCGs.

Although the star formation rate in BCGs is lower than pure cooling models predict, an enhanced star formation is observed in the BCGs of many clusters (e.g. Egami et al. 2006a; Donahue et al. 2010; Hicks, Mushotzky & Donahue 2010; Liu, Mao & Meng 2012; Fogarty et al. 2015), which correlates with the gas properties of the host cluster. For example, Wang et al. (2010) find that when comparing optically, and X-ray, selected BCGs, along with non-BCGs, that only X-ray selected BCGs show an enhanced star formation, particularly in cool cores, suggesting that the thermodynamic state of gas is important in BCG activity. Infrared (IR) emission in BCGs, for example, is seen to anti-correlate with the X-ray cooling time in the cluster core, both in the far-IR (Rawle et al. 2012), and the mid-IR (O'Dea et al. 2008). Hoffer et al. (2012) find that below an central gas entropy of 30 keV cm^2, BCGs are more likely to show an UV excess and enhanced mid-IR emission. This apparent entropy threshold is in agreement with Rafferty, McNamara & Nulsen (2008), who find optically blue cores only in clusters where the central entropy is below 30 keV cm^2, and Cavagnolo et al. (2008) who find that strong Hα and radio emission is only present in BCGs below this same entropy. Enhanced Hα and radio emission below this critical entropy suggests that both star formation and AGN activity in BCGs result from the same source, specifically cooled intracluster gas. This is further supported by the strong observational connection between optical lines in BCGs and the presence of colder gas phases traced by CO (Edge 2001; Salomé & Combes 2003), atomic lines in the FIR (Edge et al. 2010; Mittal et al. 2012), warm molecular gas (Edge et al. 2002; Egami et al. 2006b; Donahue et al. 2011) or dust (Edge et al. 1999; Rawle et al. 2012).

The location of the BCG relative to the X-ray emission also appears to be important in terms of BCG activity, where throughout the paper we use the term 'activity' to refer to either, or both, star formation and AGN activity, unless otherwise noted. In Stott et al. (2012) for example a correlation between the radio loud fraction of BCGs and proximity to X-ray centroid is seen. Crawford et al. (1999) find that BCGs with emission lines have smaller separations between their position and the X-ray centroid than BCGs without lines. Similarly Sanderson, Edge & Smith (2009) find that all the LoCUSS BCGs with optical emission-lines are within 15 kpc of the X-ray centroid and a close correspondence between Hα and radio emission and BCG/X-ray offset exists. These observations hint towards a strong association between activity in the BCG and its proximity to the centre of the cluster potential.

The primary goal of this paper is to use optical, mid-IR and UV survey data to investigate what extent correlations exist between BCG photometric colours and BCG activity. These correlations may be manifested as colour deviations from those of the bulk population of passive BCGs. With the advantage of a large sample of $\sim$1000 clusters, the aim is to investigate what proportion of BCGs, selected on host cluster X-ray emission alone, show signs of activity and determine how effectively we can detect active BCGs through photometry. In addition, we explore how, if at all, this relates to the overall X-ray properties of the cluster.

The organization of this paper is as follows: we introduce the cluster sample and details of the photometric surveys in Section 2. We present our analysis, results and discussion in Section 3 and conclude with a summary of the main results in Section 4. Throughout this paper we use AB magnitudes, except for the *WISE* data which uses Vega, and assume a standard cosmology of $H_0 = 72\,\mathrm{km\,s^{-1}\,Mpc^{-1}}$, $\Omega_M = 0.27$ and $\Omega_\Lambda = 0.73$.

2 THE DATA

2.1 The cluster sample

Our cluster sample consists of 981 X-ray selected clusters between $0.03 < z < 0.5$. The sample was drawn from a systematic investigation into the *ROSAT* All-Sky Survey (RASS) Bright Source Catalogue, BSC (Voges et al. 1999). Included in this are all published samples within the PanSTARRS-1 3π footprint, namely the Brightest Cluster Sample, BCS (Ebeling et al. 1998), the extended Brightest Cluster Sample, eBCS (Ebeling et al. 2000), the *ROSAT* ESO Flux Limited X-ray survey, REFLEX (Böhringer et al. 2004), the Northern ROSAT All-Sky Galaxy Cluster Survey, NORAS (Böhringer et al. 2000) and the Massive Cluster Survey, MACS (Ebeling, Edge & Henry 2001; Ebeling et al. 2007, 2010). We have also included all cluster identifications of RASS Bright Source Catalogue sources below the flux limits of these published surveys. The sky coverage of these additional clusters is not uniform due to variation in the exposure time and Galactic column density, but this spatial incompleteness does not affect any particular class of cluster more than another. Therefore, while the fainter clusters are incomplete and do not constitute a flux-limited sample, we can still use these clusters as a fair sample of the overall population. The relatively short duty cycle of an AGN, or a burst of star formation activity, within a BCG means that we need to maximize the parent sample we study in order to capture a meaningful number of these rare events. With X-ray luminosities ranging over two dex, but with a median $L_X \sim 2 \times 10^{44}\,\mathrm{erg\,s^{-1}}$, the sample covers a broad range of cluster mass, whilst still including only massive clusters (i.e. not groups). The redshift and X-ray luminosity distribution of our sample is given in Fig. 1. The X-ray luminosities are all drawn from the RASS, corrected for Galactic absorption and are quoted in the band 0.1–2.4 keV. We stress that from Fig. 1 it is evident that the

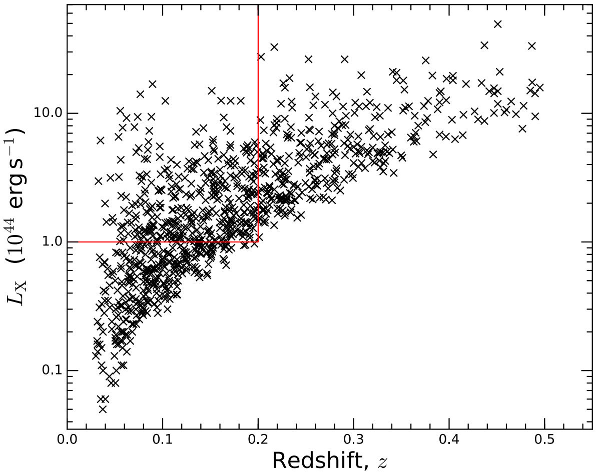

Figure 1. The RASS 0.1–2.4 keV X-ray luminosity and redshift for each of the 981 clusters in this sample. The solid (red) lines enclose the clusters selected in our 'X-ray luminosity complete' subsample.

highest X-ray luminosity clusters in our sample cover the full redshift range.

2.2 X-ray photometry: RASS

The count rates were recorded by the PSPC in channels 11–235 ('broad-band') during the RASS. These were then converted to unabsorbed X-ray fluxes in the 0.1–2.4 keV band by convolving the cluster X-ray emission with the PSPC detector response function. In this process, the cluster emission is modelled as a hot thermal plasma, characterized by metallicity (frozen at 0.3 Solar) and an intra-cluster gas temperature kT. Since the latter has not been measured for the vast majority of the clusters in our sample, it was estimated iteratively, from the observed redshift and the inferred bolometric X-ray luminosity in the cluster rest-frame, using the L_X-kT relation of White, Jones & Forman (1997). In order to correct for absorption by Galactic gas we adopt the n_H column densities compiled by Dickey & Lockman (1990). In practice, this process for translating counts to fluxes is performed as an interpolation in three dimensions (n_H, kT, z).

We have included all cluster identifications of RASS Bright Source Catalogue (Voges et al. 1999) sources below the flux limits of the published RASS cluster catalogues. However, as the RASS Bright Source Catalogue source detection was optimised for point sources, the count rate estimates from it may underestimate the counts from extended sources. The magnitude of this effect was investigated by Ebeling et al. (1998) as a function of extent and found to be significant (a factor of >1.3) in the most extended sources. We therefore make a statistical correction for the missing extended flux from the unpublished clusters by determining the ratio of count rates for the brightest clusters (the ratio of BCS and eBCS rates to the BSC rates) as a function of redshift. Above our redshift lower limit of $z = 0.03$ this ratio is at most a factor of 2.5, with an average of 1.2 for $z > 0.05$. The X-ray morphology of each individual cluster however is not accounted for in this correction, hence the flux of a few of the most nearby, most extended systems is likely underestimated.

2.3 Spectroscopic data

The optical spectroscopy for the BCGs in the sample are drawn from a wide range of sources. The bulk of this comes from the nearly complete follow-up of the BCG sample by Crawford et al. (1999), the large spectroscopic surveys by the Sloan Digital Sky Survey (York et al. 2000) and the 6dF Galaxy Redshift Survey (Jones et al. 2004), a VLT FORS survey of BCGs in REFLEX (Edge et al., in prep) and any other spectra in the literature. In total, we have reliable spectra, sufficient to detect optical emission lines, for 73 per cent of the sample.

2.4 Optical photometry: Pan-STARRS

The Pan-STARRS, PS1 3π survey (Tonry et al. 2012) is a wide-field photometric survey in the optical g, r, i, z and y bands. Covering the entire sky north of a Declination of $-30°$, the survey is conducted with the 1.8 m PS1 telescope in Hawaii, with an imaging pixel resolution of 0.25 arcsec per pixel. Using postage stamps from the PV3 data release, we performed aperture photometry on the *griz* bands using SExtractor (Bertin & Arnouts 1996) – running in dual mode with the i-band as the detection image (due to red-sensitive nature of the instrument). The inbuilt CLASS_STAR function was used for star–galaxy separation with a very conservative cut of <0.95 applied, (where 1 is a star and 0 is not), as the misidentification of faint galaxies as stars was more problematic than stellar contamination in this work. Magnitudes are given by the MAG_AUTO parameter, which measures the flux within a flexible elliptical aperture with a Kron radius (Kron 1980), and colours are derived from the MAG_APER parameter, with a fixed circular aperture.

An aperture diameter of 4 arcsec was used to measure colours. This is intentionally small, minimizing contamination from source blending in the dense cluster environment. This is supported by a χ^2 test which revealed apertures of this size minimized the scatter in the colour–magnitude relation. Metallicity (or age) induced colour gradients across galaxies are known to exist (Cardiel, Gorgas & Aragon-Salamanca 1998), so in order to quantify the effect of aperture size on colours, the 40 lowest redshift BCGs (median $z = 0.035$), which generally have the largest angular size on the sky and hence should represent the most extreme cases, were measured at aperture diameters of 4, 15, and 30 arcsec. In the case of the most extreme difference, that is between the (g–r) colour measured in a 30 arcsec and 4 arcsec apertures, (corresponding to median angular diameters of 20.5 kpc and 2.7 kpc, respectively), a median/mean colour difference of only 0.04 mag was measured, which has a negligible effect on our analysis.

Throughout this paper Galactic reddening corrections are made using the Galactic Extinction calculator available through the NED,[1] based on the Schlafly & Finkbeiner (2011) extinction maps. And where needed, K-corrections are made assuming a simple stellar population model (Bruzual & Charlot 2003) with solar metallicity, a Chabrier Intial Mass Function, formation at $z = 3$ and subsequent passive evolution.

2.4.1 Identifying the BCG

The identification of the BCGs was made via a visual inspection in the Pan-STARRS 3π imaging. The selection was primarily based on their morphology and centrality, looking for the visually most

---

[1] http://ned.ipac.caltech.edu/forms/calculator.html

extended galaxy – often with a cD-like profile – at the centre of the galactic distribution. As such, the BCG need not necessarily be photometrically the brightest galaxy. When the choice of galaxy was ambiguous, the candidate best aligned with the X-ray emission was selected. Visual identification, although time consuming, is probably still the most reliable method, minimizing issues with projection. Visually inspecting each image also aided in the identification of misclassified X-ray point sources in the sample, since these generally lack the visually obvious galactic overdensities characteristic of clusters.

Lauer et al. (2014) find that if taking the literal definition of a BCG as the brightest galaxy, then 12 per cent of local clusters have a BCG >500 kpc from the X-ray centre. They conclude these are likely drawn into a cluster from recent merger events, as modelled by Martel, Robichaud & Barai (2014). However, as we are interested in the interplay between the BCG and its traditionally-central environment, we redefine our BCGs as the brightest, most extended, central galaxy.

2.5 Mid-IR photometry: *WISE*

The *Wide-field Infrared Survey Explorer* (*WISE*) (Wright et al. 2010) has covered the whole sky in the mid-IR at 3.4, 4.6, 12 and 22 µm. From the AllWISE Source Catalogue we extract photometry for our BCG sample in the *W*1, *W*2 and *W*3 bands at 3.4, 4.6 and 12 µm, respectively. The *WISE* source closest to the BCG position is selected, which is within 1 arcsec for 79 per cent of BCGs, 2 arcsec for 94 per cent of BCGs and within 6 arcsec for all BCGs. We do not perform any Galactic extinction corrections as this is negligible for mid-IR observations (Cardelli, Clayton & Mathis 1989).

The full BCG sample is well detected in *W*1 and *W*2, with a Signal to Noise, $S/N > 3$ for all observations. At 12 µm (*W*3) however some sources are not detected due to the flux limit of *WISE*. We thus restrict our *W*3 analysis to detections with $S/N > 3$ and find that the number of robustly detected BCGs in *W*3 is 552 (56 per cent of total sample size).

2.6 UV photometry: *GALEX*

The *Galaxy Evolution Explorer* (*GALEX*) (Martin et al. 2005) is a space based observatory imaging in two ultraviolet bands, the far-UV (FUV) at 1350–1780 Å and the near-UV (NUV) at 1770–2730 Å. We used the aperture photometry available from the *GALEX* catalogue[2] and extracted any source within six arcsecs of our BCG position. If multiple observations were returned, we attempted to maximize the signal to noise by taking the observation with the longest exposure time – unless the next longest exposure was more central and within 2/3 of the highest exposure time, since the PSF is poorer with radius from the centre in the *GALEX* field of view. We correct for Galactic extinction assuming $A_{\rm FUV} = 2.5\,A_V$ and $A_{\rm NUV} = 3.25\,A_V$ (Hoffer et al. 2012).

The *GALEX* catalogue is compiled of observations from numerous nested *GALEX* surveys, which vary in sky coverage and depth, none of which are full sky and hence our sample is far from complete in the UV. The widest survey, the All-sky Imaging (AIS), (which despite the name covers only 26 000 deg^2 of the sky) has typical exposure times of only 100s, which are insufficient for a robust detection for most of our redshift range. Hence, despite the catalogue returning a detection for 541 of our BCGs within 6 arcsec, when we restrict our analysis to detections with $S/N > 3$, the number of galaxies reduces to 245 BCGs (∼25 per cent of the total sample).

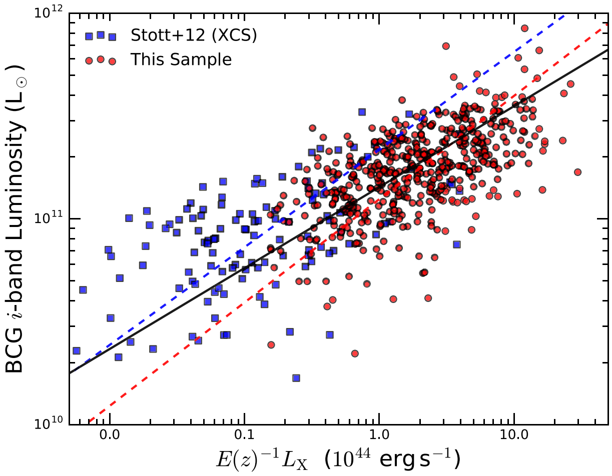

Figure 2. The *i*-band luminosity of BCGs, against the 0.1–2.4 keV X-ray luminosity of the host cluster. The (red) circles represent our cluster sample and the (blue) squares represent the groups/clusters from Stott et al. (2012) – corrected to have optical and X-ray measurements comparable to our own. The dashed lines represent the BCES bisector best fits to the sample of corresponding colour and the solid black line represents a BCES bisector fit to the combined data sets.

2.7 Radio: NVSS

The NRAO VLA Sky Survey (NVSS) (Condon et al. 1998), operating at 1.4 GHz, covered the entire sky north of a Declination of −40° and thus provides observations of our entire sample. We use the NVSS Source catalogue[3] to extract the photometry for the nearest detection within 45 arcsec of the BCG position. Whilst the spatial resolution of NVSS does not permit us to attribute a radio detection to the BCG with certainty, BCGs are the most likely cluster galaxy to host a radio-loud AGN (Burns, Gregory & Holman 1981; Valentijn & Bijleveld 1983; Burns 1990; Best et al. 2007) and hence we assume any radio detection to be associated with the BCG. We find 512 BCGs with an associated radio detection, corresponding to a radio detection rate of 52 per cent, this is comparable to the ∼60 per cent detection rate of Hogan et al. (2015), but, logically, less given our sample goes to higher redshift.

3 RESULTS

3.1 Optical analysis and results

3.1.1 BCG luminosity

We begin our optical analysis by comparing the properties of the BCG with those of the host cluster, as seen in Fig. 2. We find that the BCG *i*-band luminosity is weakly correlated with the host cluster X-ray luminosity, such that, whilst for any individual BCG the scatter is significant, we do see a general trend in which the brighter BCGs tend to reside in the more X-ray luminous clusters. This reinforces previous results showing a correlation between optical BCG luminosity and cluster X-ray luminosity (e.g. Edge 1991; Stott et al. 2012). We conclude that, given that optical luminosity

---

[2] http://galex.stsci.edu/GalexView/

[3] www.mrao.cam.ac.uk/projects/surveys/nrao/NVSS/NVSS.html

traces stellar mass and cluster X-ray luminosity traces the cluster mass, the most massive BCGs tend to belong to more massive clusters. This interpretation is supported by the results of Stott et al. (2010) and Lidman et al. (2012) who derive BCG stellar masses and cluster masses from BCG Near-IR luminosities and cluster X-ray temperatures, respectively, (which are both more reliable tracers of mass). Additionally, a positive correlation between BCG luminosity and the cluster velocity dispersion – another tracer of cluster mass – has also been observed (Whiley et al. 2008; Lauer et al. 2014).

In Fig. 2 we plot the corrected values of L_{X} and L_{i} from (Stott et al. 2012, hereafter S12) alongside our own for comparison. The S12 L_{i} values are derived from SDSS model magnitudes, which have systematically brighter fluxes than measured through our own PS1 photometry by a few tenths of a magnitude. Since this offset in BCG flux is uniform with redshift we apply a correction of the median value of 0.4 mag to the S12 values. Additionally we apply a correction in the S12 L_{X} values, (taken from the XCS; Mehrtens et al. 2012), from bolometric values to that of 0.1–2.4 keV. This is achieved using the ratio of 0.1–2.4 keV flux to bolometric flux, as a function of temperature, and the XCS temperature values from S12. Applying a linear regression BCES bisector fit (Isobe et al. 1990) to the points we find,

$$\log_{10}(L_i) = \alpha \log_{10}(E(z)^{-1} L_{\mathrm{X}}) + \beta, \qquad (1)$$

where L_i is the BCG i-band luminosity ($\mathrm{L}_{\odot}$), L_{X} is the 0.1–2.4 keV X-ray luminosity (10^{44} erg s^{-1}) and $E(z) = [\Omega_m(1+z)^3 + \Omega_\Lambda]^{1/2}$ with $\alpha = 0.48 \pm 0.08$ and $\beta = 11.34 \pm 0.08$ for the S12 sample, $\alpha = 0.50 \pm 0.04$ and $\beta = 11.09 \pm 0.02$ our sample and $\alpha = 0.39 \pm 0.04$ and $\beta = 11.15 \pm 0.09$ for the combined samples. Hence we find, when comparing the best-fitting lines to this sample and the S12 sample, that the slopes are consistent but there is an offset in the normalization. The interpretation is that this reflects the differing sample selection – specifically that the XCS sample is dominated by low mass galaxy groups/clusters and our sample is dominated by massive clusters. We find the slope for the combined samples is flatter than either separate sample, suggesting a possible flattening of the relation in low mass haloes. This is perhaps driven by a lower prevalence of AGN feedback in low mass haloes. Hence the stellar mass growth of their central galaxies is not as effectively truncated.

3.1.2 *Cluster red sequence*

The cluster red sequence, the observed linear relationship between magnitude and colour for cluster galaxies, was selected using a multicolour band approach. First, a conservative colour cut is applied around the expected red sequence colour given its redshift. Then magnitudes are binned and the median colour selected for each bin. A further colour cut is applied around these median colours and a linear fit is then made to these sources, constituting the initial red sequence fit. The colour index spanning the rest-frame 4000 Å break and the adjacent redder-colour index are then cross-matched, where only sources that fit the initial red sequence in both colour bands are classified as red sequence galaxies. Because cluster early type galaxies are the reddest, brightest galaxies at a given redshift, this stage reduces contamination of the red sequence as spanning the 4000 Å break provides the most significant contrast with field galaxies. The linear fit and cross-matching process is then repeated iteratively, decreasing the colour clipping each time, until a final clip of ±0.1 mag around the red sequence best fit is made and defined as our cluster red sequence. Our analysis of the colour-magnitude relation is restricted to a radius of 0.5 Mpc around the BCG position.

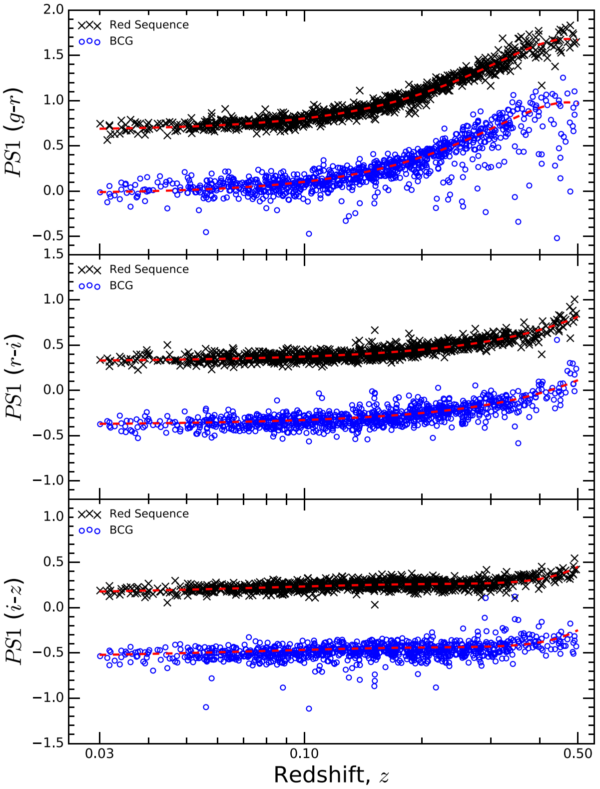

Figure 3. PS1 g–r (top panel), r–i (middle panel) and i–z (bottom panel) colours, against redshift. The (black) crosses show the colour of the cluster red sequence, measured at a flux of 19th magnitude for each cluster. The (blue) open circles show the colour of the BCG for each cluster, but corrected to be at a flux of 19th magnitude also. The BCGs (open circles) have been artificially offset by −0.7 mag for visual clarity. The upper (red) dashed line in each panel shows a best fit to the red sequence. These exact same lines are offset by −0.7 mag also, forming the lower dashed lines, this is to show the reader that the bulk population of BCGs lie on the cluster red sequence as expected for a passive galaxy.

In Fig. 3 we explore the PS1 g–r, r–i and i–z colours of the red sequence, measured at a fixed flux of 19th magnitude and how this relates to redshift. We measure this at magnitude 19 as the red sequence generally pivots about this value, thus minimizing the colour error due to the uncertainty of the red sequence slope. The small level of scatter of this distribution illustrates the homogeneity of the cluster red sequence population, despite the different cluster environments and masses in our sample (Andreon 2003). The observed evolution with z is dominated by the transition of the 4000 Å break through the photometric bands (i.e. the redshift evolution that one would K-correct for), and also the relative change in position of 19th magnitude along the red sequence gradient (which typically goes redder at the bright end).

The tight relationship in red sequence colour with redshift means the colour of a cluster's red sequence can provide an estimate for its redshift. In Fig. 4 we test this by comparing the redshift predicted by its red sequence g–r colour, against the actual redshift, for our cluster sample. We find that the predicted and actual redshift agree to within 0.025 at 1σ. The increased scatter at higher z is due to the increased difficulty in reliably selecting the red sequence. At high redshift, ($z > 0.3$), only the very brightest few red sequence galaxies are detected, giving few points on which to select and extrapolate the red sequence. The largest source of uncertainty is correctly sampling the red sequence slope, which is used when evaluating the

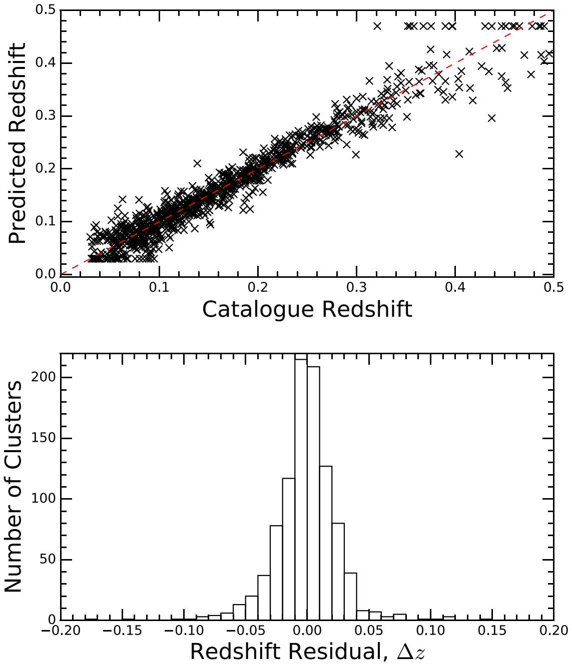

Figure 4. Top: the predicted redshift, derived from the g–r colour of the red sequence, against the catalogued redshift for each cluster. Bottom: the redshift residuals between the predicted and actual redshifts. The distribution has a mean at zero and standard deviation of 0.025 . At higher redshifts there are sometimes very few red sequence galaxies above the PS1 flux depth, and as a result the true red sequence is difficult to select correctly; this explains those cases where the predicted redshift and actual redshift significantly deviate. Also, any red sequence colour above our peak in the curve results in a predicted redshift corresponding to the sample maximum at ∼0.46.

g–r offset. Poor selection of the red sequence at high z accounts for those clusters with significant redshift residuals.

The colour of the cluster red sequence provides a standard for the colour one would expect for a passively evolving galaxy on the red sequence. The equivalent colour of the BCG can thus be compared to this and hence used to determine whether deviations from passivity exist for these galaxies. In addition to this, analysis of red sequence was a useful tool in identifying and removing any misclassified source in the X-ray catalogue. For example, a number of sources in the initial sample were point sources, such as AGN and white dwarfs. The lack of red sequence in such cases made identification, and thus removal, of these simple.

3.1.3 BCG colour

In Fig. 3 we also display the PS1 g–r, r–i and i–z colours of the BCG in each cluster, corrected to be at the same flux as the red sequence. We see that the BCG colour evolution generally follows the same trend with redshift as the red sequence, indicating that most BCGs lie on the red sequence. As with the red sequence colours, the BCGs form a fairly tight relation suggesting BCGs are generally a fairly homogeneous galaxy population. This is to be expected if you consider BCGs to be quiescent galaxies that formed their stellar populations at $z > 2$, like the other cluster members. However, we see also a significant number of BCGs with optical colours that differ from that of the bulk, passive population, particularly in g–r.

In Fig. 5 we show the g–r colour offset, defined as the colour difference between the BCG and the red sequence at the same flux. There are a number of BCGs which have g–r colours significantly bluer than the red sequence galaxies, which could be indicative of star formation and/or AGN activity. To explore this further we split our BCG sample by emission line status as both star formation and AGN activity lead to optical emission lines in galaxies. We divide our BCGs into: those with strong emission lines (Hα slit flux $>10^{-15}$ erg cm^{-2} s^{-1}), those with weak emission lines ($<10^{-15}$ erg cm^{-2} s^{-1}), those with no lines, and those without any spectral data available.

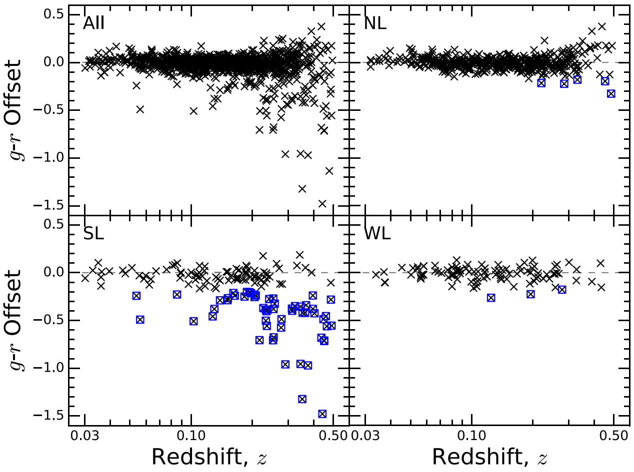

Figure 5. Each panel shows the BCG g–r colour offset – defined as the difference between the BCG and red sequence colour – against redshift. The panel is split into: full sample (top left), non line emitters (top right), strong line emitters (bottom left) and weak line emitters (bottom right.) The (blue) squares indicate those BCGs with colour offsets in excess of $>2.5\sigma_p$ from zero, where σ_p is the scatter of the non-line emitters.

We see from Fig. 5 there is a clear connection between g–r colour offset and line status with most blue BCGs also showing strong emission lines. This is in stark contrast to BCGs without emission lines, which have a mean g–r offset of zero, as expected for passive galaxies. If we thus assume the non line-emitting BCGs are representative of the quiescent population, we can use these to estimate the general scatter in colour and hence quantify what constitutes a significant deviation in colour from passivity. We find a standard deviation of $\sigma_p = 0.07$ mag for the non line-emitting (‘passive’) BCGs.

Defining our threshold for BCG activity as a colour offset in excess of $2.5\sigma_p$, we find that 8 per cent of BCGs exhibit significantly blue colours and as such are classed as ‘active’. Of the strong line emitting subsample, 39 per cent of BCGs show a g–r offset $>2.5\,\sigma_p$ and the mean offset is −0.19 mag. In fact, all the BCGs with g–r offsets <-0.5 mag are either strong line emitters or have no available spectra (and are likely strong line emitters themselves). The strong connection between optical colour and line status is indicative that these BCGs are optically blue because of activity in the BCG. Note that we have manually investigated the colour magnitude diagrams of all apparently blue BCGs to rule out incorrect selection of the red sequence as an origin for the offset in g–r, in addition to double checking our BCG selection was correct. A summary of the fraction of optically blue BCGs as related to line status is provided in Table 1.

It is interesting to note that whilst optical emission lines are indicative of activity, ∼60 per cent of those BCGs with emission lines do not show up as optically blue. In most cases this is likely a result of the fact that obscured star formation and/or AGN activity can lead to ionization of the gas, visible as strong emission lines,

Table 1. Percentage of BCGs with an optical (Opt.), mid-IR or UV colour offset $>2.5\sigma_p$, where σ_p is the scatter for the non-line emitting (passive) BCGs. The percentage of BCGs with a significant offset in any one of the colours is given in the 'Combined' column. The 'Radio' column indicates a detection only, not an excess. Percentages are presented as fractions of the full sample (All) and strong line emitting (SL), weak line emitting (WL) and non-line emitting (NL) subsamples.

	BCGs (No.)	Opt. (per cent)	MIR (per cent)	UV (per cent)	Combined (per cent)	Radio (per cent)
All	981	8	9	4	14	52
SL	144	39	35	19	51	84
WL	100	3	8	3	11	43
NL	476	1	3	1	5	43

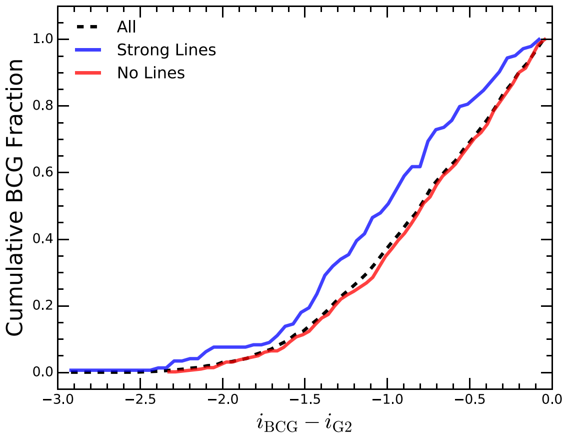

Figure 6. The cumulative fraction of clusters as a function of the *i*-band magnitude difference between the BCG and *G*2, the 2nd ranked cluster red sequence galaxy.

whilst having minimal influence on the continuum emission, and hence colour, of the overall galaxy. Additionally, the optical line emission associated with the BCG may result, not from ionizing stars or AGN, but from ionization at the hot/cold interface between clouds of cold molecular gas and the surrounding hot ICM in the cores of cool core clusters (Ferland et al. 2009; Fabian et al. 2011; Hamer et al. 2016). Aperture effects may also be a contributing factor, whereby the photometry and spectroscopy are probing different regions of the BCG. As an aside, it should be noted that the fact some BCGs are optically blue has implications regarding optical cluster algorithms, which often select the BCG assuming a BCG colour on the red sequence.

3.1.4 *BCG dominance*

Next we investigate the connection between the emission line status of the BCG, and its dominance relative to its companions in the cluster. In Fig. 6 we show the cumulative fraction of BCGs, as a function of the magnitude difference between the BCG and the 2nd ranked galaxy on the red sequence, *G*2. A connection appears to exist between the luminosity dominance of the BCG and its emission line status, with a higher fraction of strong line emitting BCGs showing a large magnitude separation between itself and *G*2 compared to those with no lines. This observation is consistent with implications from the literature, that is, that BCGs with emission lines trace cool core clusters (Heckman 1981; Hu, Cowie & Wang 1985; Johnstone, Fabian & Nulsen 1987; Heckman et al. 1989; Crawford et al. 1999; McDonald 2011), thus tend to be located at the very centre of the cluster potential (Sanderson et al. 2009) and the observation that BCGs are more likely to be cD galaxies when in close proximity to the cluster centre (Lauer et al. 2014). This also agrees with Smith et al. (2010) which demonstrated a direct association between the BCG dominance and the central gas density profile of the cluster, specifically that clusters hosting a high luminosity gap also host strong cool cores.

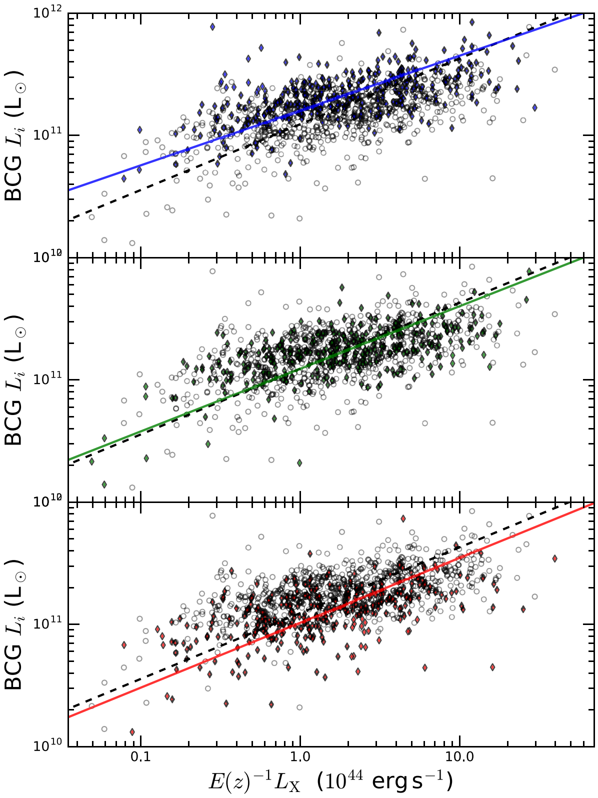

Figure 7. The PS1 *i*-band luminosity of the BCG, against the 0.1–2.4 keV X-ray luminosity of the host cluster. The sample is split equally into three based on BCG dominance, described by the difference in magnitude between the BCG and the second ranked galaxy. The filled diamonds in the top panel correspond to BCGs in the top tier – that is, the BCGs with the biggest magnitude difference – the filled diamonds in the second panel correspond to the middle tier and the filled diamonds in the bottom panel correspond to the bottom tier. The open circles show the full sample to aid visual comparison. The dashed line indicates the best fit, made using a BCES bisector fit, to the full sample, the solid line in each panel indicates a best fit to the filled diamonds of that panel.

BCG dominance is also explored in Fig. 7 – here we divide the full sample into three based on the magnitude difference between themselves and *G*2 and find that the most dominant BCGs are systematically more luminous than other BCGs in clusters of similar X-ray luminosity, with the converse being true for the least dominant BCGs. This supports the notion that the magnitude difference is dominated by the brightness of BCGs themselves and not just reflective of a deficit in the brightness of *G*2 in these particular systems. In principle, the apparent correlation between BCG $L_{\rm i}$ and cluster $L_{\rm X}$ that is seen could be explained by the association between cool core clusters and an enhanced BCG dominance – whereby the cool core nature of a cluster leads to an enhancement in both the *i*-band and X-ray brightness. However the existence of this correlation in all three subsamples, even in the lowest third by luminosity gap, supports the interpretation that this is not a significant factor here.

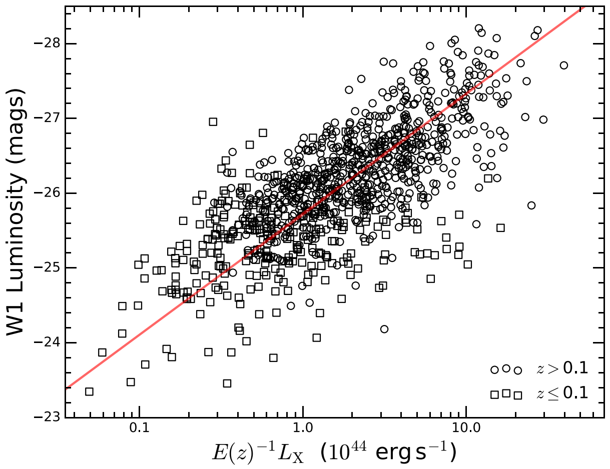

Figure 8. The *WISE* *W*1 (3.4 µm) luminosity of the BCG against the 0.1–2.4 keV X-ray luminosity of the host cluster. The (red) dashed line indicates our best fit, made using a BCES bisector fit.

3.2 Mid-IR analysis and results

3.2.1 *BCG luminosity*

In Fig. 8, we find that the BCG *WISE* *W*1-band luminosity correlates with the X-ray luminosity of the host cluster. This reinforces the results from our optical analysis (Fig. 2), but with less scatter in the mid-IR. The interpretation is that BCGs with higher stellar mass tend to reside in more massive clusters, as suggested from near-IR observations also (e.g. Lin & Mohr 2004; Stott et al. 2008, 2010; Lidman et al. 2012). Applying a linear regression BCES bisector fit (Isobe et al. 1990) we find,

$$L_{W1} = (-1.61 \pm 0.02)\log_{10}(E(z)^{-1}L_X) - (2.57 \pm 0.02), \qquad (2)$$

where L_{W1} is the BCG *W*1-band luminosity (mag), L_X is the X-ray luminosity (10^{44} erg s^{-1}) and $E(z) = [\Omega_m(1+z)^3 + \Omega_\Lambda]^{1/2}$.

3.2.2 *BCG colours*

In the IR the contribution from stellar mass decreases with wavelength, becoming more strongly dependent on dust emission at larger wavelengths. Hence in the mid-IR, particularly at 12 µm, we are sensitive to reprocessed emission from dust. An active BCG, with recent star formation and/or AGN activity, is consequently expected to show an excess in mid-IR emission as the dust gets heated by the hot young stars and/or AGN. The colour of an active galaxy would as a result be redder than that of a passive galaxy, because the dust contribution is more significant in the redder band. As AGN output can heat dust to $T > 80$ K, the most extreme cases of mid-IR excess are likely due to AGN contribution.

All BCGs are well detected in *W*1 and *W*2, but only 552 BCGs are robustly detected (i.e. $S/N > 3$) in *W*3, due to the declining continuum in the SEDs of passive galaxies with respect to wavelength in the IR. In Fig. 9 we show the *W*1, *W*2 and *W*3 flux against redshift, with arrows indicating upper limits (i.e. where S/N < 3). The proportion of BCGs detected in *W*3 is clearly a function of redshift and beyond $z \sim 0.15$ the quiescent BCG population is not well sampled. Fortunately BCGs with a clear *W*3 excess continue to have robust detections across the redshift range and hence we expect this to have minimal effect on the detection of active BCGs. In order to define a *W*3 excess however this does require an extrapolation of the *W*3 flux–redshift relation for the bulk population of passive BCGs. First a best fit is made to the bulk population, (ignoring those with clear excess), for *W*1 and *W*2. From the figure we see the relation between these two is very similar and the relation for *W*3 is expected to be similar also. Hence using the *W*2-*z* relation as a template, we iteratively determine the best fit to those BCGs with $S/N > 3$ and $z < 0.15$, again ignoring the BCGs with a clear *W*3 excess, and extrapolate this relation to the higher *z*, where our bulk quiescent population is lost to the flux limit.

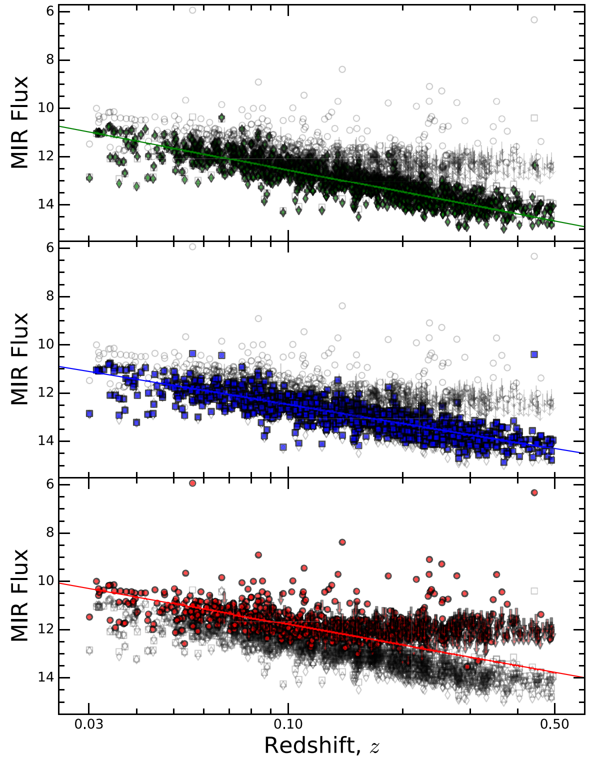

Figure 9. The *WISE* fluxes of our BCGs against redshift. The *W*1 (3.4 µm) fluxes are given by the (green) diamonds in the top panel, the *W*2 (4.6 µm) fluxes by the (blue) squares in the middle panel and the *W*3 (12 µm) fluxes by the (red) circles in the bottom panel. The grey points correspond to the values of the other bands with their respective symbols. Any points given as arrows indicate limiting magnitudes with poor signal to noise (S/N < 3). Clearly from this figure the depth of *W*3 is insufficient to probe the quiescent galaxy population beyond $z \sim 0.1$, but crucially for our study, those with a strong *W*3 excess continue to show up at least until $z = 0.5$. The solid lines show the respective best-fitting trends to the bulk quiescent population of BCGs, in the case of *W*3, this is extrapolated from $z \leq 0.1$.

We can also deduce from Fig. 9 that *WISE* can measure BCG fluxes beyond $z > 0.5$. In *W*1 and *W*2 it appears we can continue detecting the bulk population further, but crucially for studies of activity, we expect to be able to measure excesses even further. This will be a useful factor when comparing BCG properties of the low-*z* Universe to those at higher *z*. For instance, the most extreme systems at $z > 0.5$, such as the Phoenix cluster ($z = 0.598$; McDonald et al. 2012), that is an AGN-dominated BCG with *W*3 magnitude of 7.93 mag, would be detectable with *WISE* to at least $z = 1.5$. So, while the less active AGN are lost at $z > 0.3$, we can still identify the most active systems in any sample, such as the XCS (Romer et al. 2001) in the X-ray, or MaDCoWS (Stanford et al. 2014) in the mid-IR.

In order to test for a mid-IR excess we explore the mid-IR colours, *W*1–*W*2 and *W*2–*W*3. In Fig. 10 the *W*1–*W*2 ($3.6 - 4.6$µm) colour against redshift shows that the passive BCG population undergoes a peaked evolution with redshift – due to the redshift of a continuum break in the SED here. This effect has sometimes been ignored

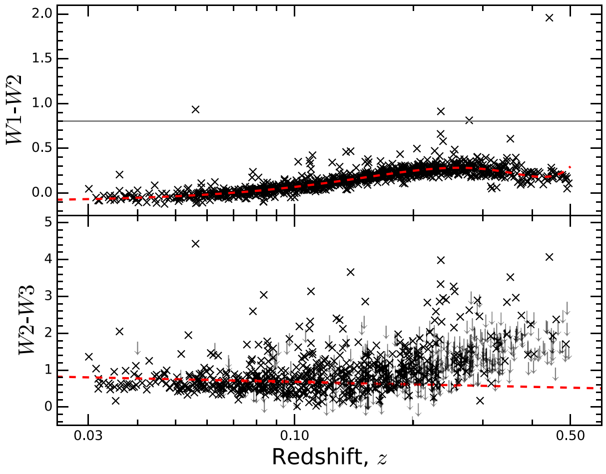

Figure 10. The $W1-W2$ ($3.4-4.6$ μm) and $W2-W3$ ($4.6-12$ μm) colour evolution of the BCGs, with respect to redshift. The grey arrows indicate sources where $W3$ S/N < 3 and the red dashed lines indicate the assumed best fit for a passively evolving galaxy (see main text). The solid grey line in the top panel indicates the selection criteria of $W1$–$W2$ > 0.8 mag for strong AGN.

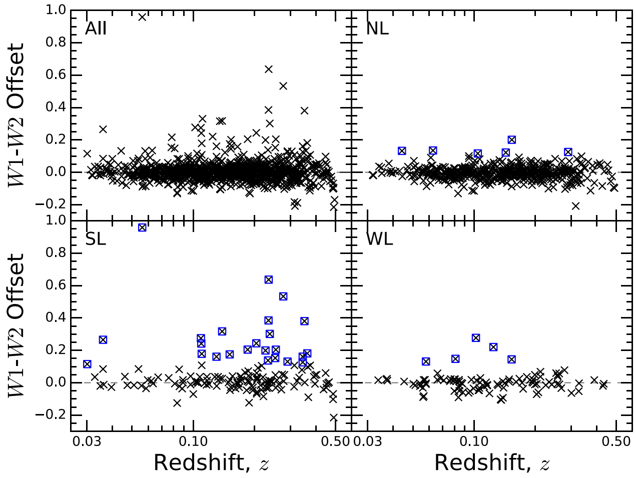

Figure 11. The *WISE* $W1$–$W2$ ($3.4-4.6$ μm) BCG colour offset against redshift. The panel is split into: full sample (top left), non-line emitters (top right), strong line emitters (bottom left) and weak line emitters (bottom right.) The (blue) squares indicate those BCGs with colour offsets in excess of $>2.5\sigma_p$ from zero, where σ_p is the scatter of the non-line emitters. Note there is another point with a $W1$–$W2$ offset of 1.78, corresponding to MACSJ0913.7+4056, which is omitted here for the sake of visual clarity.

in the literature, where conclusions are drawn from raw colours only (e.g. Quillen et al. 2008; Fraser-McKelvie, Brown & Pimbblet 2014). Fig. 10 illustrates that if using just raw colours, $W2$ excesses at redshifts below the peak are lost to the redshift relation and hence some star forming galaxies would be missed. This illustrates why one should consider a colour offset (as used here) or a normalized flux ratio (such as in Hoffer et al. 2012). Having already established most BCGs are indeed passive we can hence determine a $W1$–$W2$ colour offset by collapsing along the best-fitting line to the bulk passive trend in Fig. 10, with the offset defined as the difference in the measured colour and that predicted by this best fit.

The $W1$–$W2$ offset shown in Fig. 11 show that there are a number of BCGs which exhibit a significant offset and that these correlate with the optical emission line status. For the non-line emitting

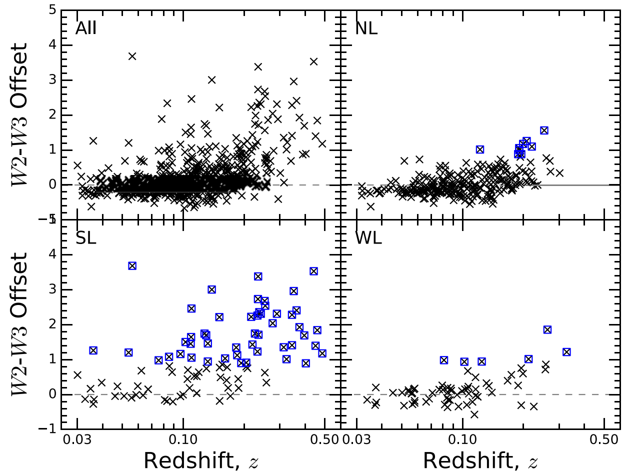

Figure 12. The *WISE* $W2$–$W3$ ($4.6-12$ μm) colour offset against redshift for BCGs with a $W3$ S/N > 3 (552 BCGs). The panel is split into: full sample (top left), non-line emitters (top right), strong line emitters (bottom left) and weak line emitters (bottom right.) The (blue) squares indicate those BCGs with colour offsets in excess of $>2.5\sigma_p$ from zero, where σ_p is the scatter of the non-line emitters.

BCGs, i.e. passive BCGs, we measure a scatter with a standard deviation, $\sigma_p = 0.04$ mag and a mean of zero. If we then define a $W2$ excess as an $W1$–$W2$ offset $>2.5\sigma_p$, we find 5 per cent of the total show an excess, increasing to 17 per cent for the subsample of strong line emitters.

Enhanced $W2$ emission is often an indicator of AGN activity in a galaxy (resulting from the nature of the power spectrum of AGN (O'Dea et al. 2008). Using the basic AGN selection criteria of $W1$–$W2$ >0.8 from Assef et al. (2013) we recover four BCGs hosting a strong AGN. These four are the BCGs of Zw 2089 (Russell et al. 2013), Cygnus-A (Russell et al. 2013), MACSJ0913.7+4056 (Hlavacek-Larrondo et al. 2013), and PKS2338+000. This allows us to determine a conservative lower limit of four BCGs hosting strong AGN in our sample (<1 per cent). However the reliability and completeness of a simple colour AGN selection method assumes highly luminous AGN only, and are calibrated on 'typical' AGN host galaxies. BCGs are anything but typical and hence it is inevitable that the host BCG has a significant contribution to the $W1$ flux, diluting the relative $W2$ excess. Hence we are almost certainly underestimating the overall AGN fraction with other AGN host galaxies just falling short of this formal selection cut. Nonetheless, this result shows that whilst ongoing strong AGN are extremely rare, the AGN duty cycle is non-zero in these galaxies.

Fig. 12 shows the $W2$–$W3$ ($4.6-12$ μm) colour offset. This is difference between the measured $W2$–$W3$ and the estimated best fit for $W2$–$W3$, given by the $W2$ best fit minus the expected $W3$ best fit. Once again we see that non-line emitting BCGs do not generally show any mid-IR excess, with a mean offset of zero, consistent with passivity. With a scatter of $\sigma_p = 0.35$ mag in the non-line emitters we find at least 8 per cent of total BCGs show a significant colour offset (i.e. an offset $>2.5\sigma_p$). This fraction is increased to 35 per cent for the strong line emitting BCGs. As expected weak line emitters behave somewhere in between, with most near zero but with a handful showing a significant offset (6 per cent). The reader should note that the apparent deficit of non-offset galaxies at high redshift is a result of the passive BCG population lacking robust detections in $W3$ at $z \gtrsim 0.15$. One should also note that the fraction of BCGs said to show a significant offset are evaluated as a proportion of

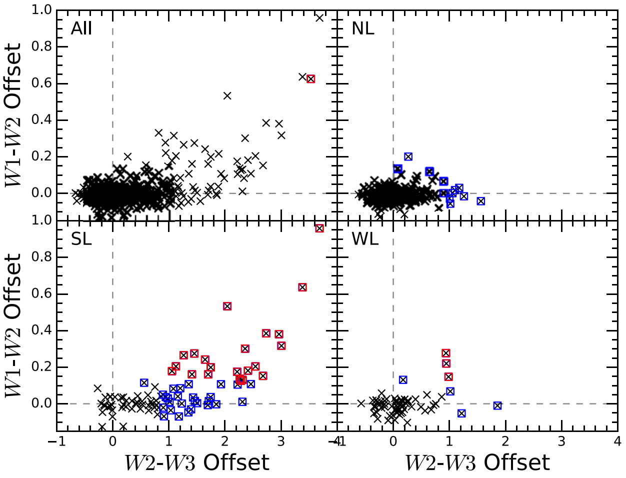

Figure 13. The $W1$–$W2$ offset against $W2$–$W3$ offset for BCGs. The panel is split into: full sample (top left), non-line emitters (top right), strong line emitters (bottom left) and weak line emitters (bottom right.) The (blue) squares indicate those BCGs with colour offsets in excess of $>2.5\sigma_p$ from zero, where σ_p is the scatter of the non-line emitters. The red squares correspond to galaxies significantly offset in both colours and thus likely indicate BCGs hosting AGN. Note there is another point with $W1$–$W2$ and $W2$–$W3$ offsets of 1.78 and 3.52, respectively, corresponding to MACSJ0913.7+4056, which is omitted here for the sake of visual clarity.

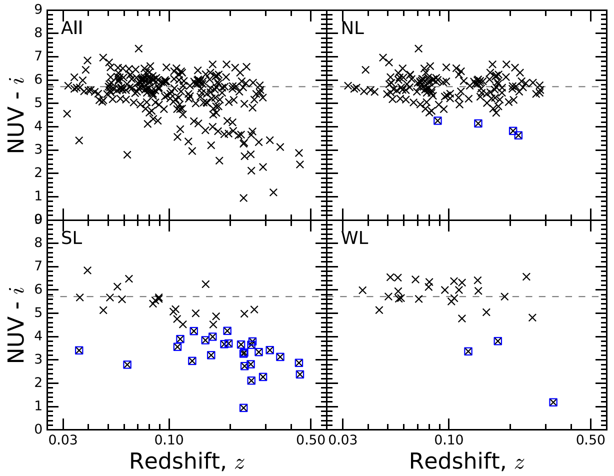

Figure 14. NUV–i against redshift for the 245 BCGs detected in the NUV with S/N >3. The dashed line indicates the median colour of the passive, non-line emitting, BCGs at 5.80 mag. We define subsequent NUV–i colour offsets relative to this line. The panel is split into: full sample (top left), non line emitters (top right), strong line emitters (bottom left) and weak line emitters (bottom right.) The (blue) squares indicate those BCGs with colour offsets in excess of $>2.5\sigma_p$ from zero, where σ_p is the scatter of the non-line emitters.

the total sample, under the assumption that the undetected BCGs are exclusively passive. This means that the fractions are in fact lower limits, since although most BCGs with mid-IR excess are still detected, there could be some BCGs with a modest, but still significant offset, where robust detections are not possible in $W3$.

In Fig. 13 we plot the $W1$–$W2$ and $W2$–$W3$ colour offsets against each other for BCGs with S/N > 3. There is a clearly a correlation between a $W1$–$W2$ offset and $W2$–$W3$ offset, with the most extreme offsets in one corresponding to the most extreme offset in the other. As discussed above, the BCGs with the largest offsets in both the mid-IR colours are likely to be a result of AGN contribution within the BCG. Whereas the BCGs with a significant offset in $W2$–$W3$, but which are do not show a significant $W2$ excess are likely to be dominated by star formation (Donahue et al. 2011). Overall, we find at least 9 per cent of our BCGs show an excess in either $W2$ or $W3$, increasing to 36 per cent for the strong line emitting subsample (see Table 1).

3.3 UV analysis and results

In the UV wavelength regime we are particularly sensitive to emission from young O and B type stars, hence recent star formation is characterized by an enhanced UV emission. We investigate the BCG NUV–i colour against redshift, (Fig. 14), in order to test for enhanced UV emission in our BCG sample. We use the i band photometry because at these redshifts it is unaffected by the shift of the 4000 Å break. There appears to be no significant redshift evolution in the NUV–i colour for the quiescent BCGs and so we define a UV offset as the difference between the measured NUV–i and the median NUV–i value of 5.80. The non-line emitting BCGs form a relatively tight cloud around this median, with a standard deviation of σ_p = 0.57 mag, consistent with passivity.

As a fraction of the 245 BCGs with robust NUV detections, we find 16 per cent, 32 per cent and 4 per cent show a significant offset, (defined as an NUV–i offset $>2.5\sigma_p$), in the full, strong line and weak line emitting samples, respectively. However we stress that the UV detections are not complete in sky coverage, or of uniform depth for those observed. Because of this we preferentially select galaxies with a UV excess. Hence we are only able to determine lower limits, as a fraction of the total BCG sample. With this in mind, we find that at least 4 per cent of BCGs show a UV excess. This fraction is increased to 19 per cent of BCGs known to exhibit strong optical emission lines and is 3 per cent for those with weak lines (as summarized in Table 1).

3.4 Comparing the optical, UV and mid-IR photometry

In Fig. 15 we display the PS1, *WISE* and *GALEX* colour offsets against one another. We see that BCGs with a significant colour offset at one wavelength are likely to, but not necessarily to, exhibit a significant offset in another. This tells us that the colours at both wavelengths are likely to be due to the same phenomena. Fig. 15 also illustrates the importance of using multiwavelength photometry in such an analysis. We see that not all colour bands measure BCG activity equally, due to the complimentary nature of different wavelength observations. Some bands are more sensitive to certain phenomena than others, and over different time-scales. In the UV for example we are especially sensitive to ongoing, unobscured star formation, whereas in the mid-IR we can measure obscured star formation/AGN activity, and over longer time-scales. Note, details on the individual clusters which have a significant colour offset(s) in their BCGs are given in Table A1.

In Fig. 15 we see only one non-line emitting BCG, that of A1704, which has a significant offset in more than one colour index, (with a significant offset in g–r, NUV–i and $W2$–$W3$). This particular galaxy has an SDSS spectra of its core, which shows no emission lines. However, the imaging clearly shows an optically blue component within the BCG, but offset from the centre of the galaxy. Our prediction is that if the spectral fibre had been placed on this region then it would likely show strong emission lines, (however projection cannot be ruled out at this stage). Optical line emission offset from the BCG has been observed in a number of cluster cores (Hamer

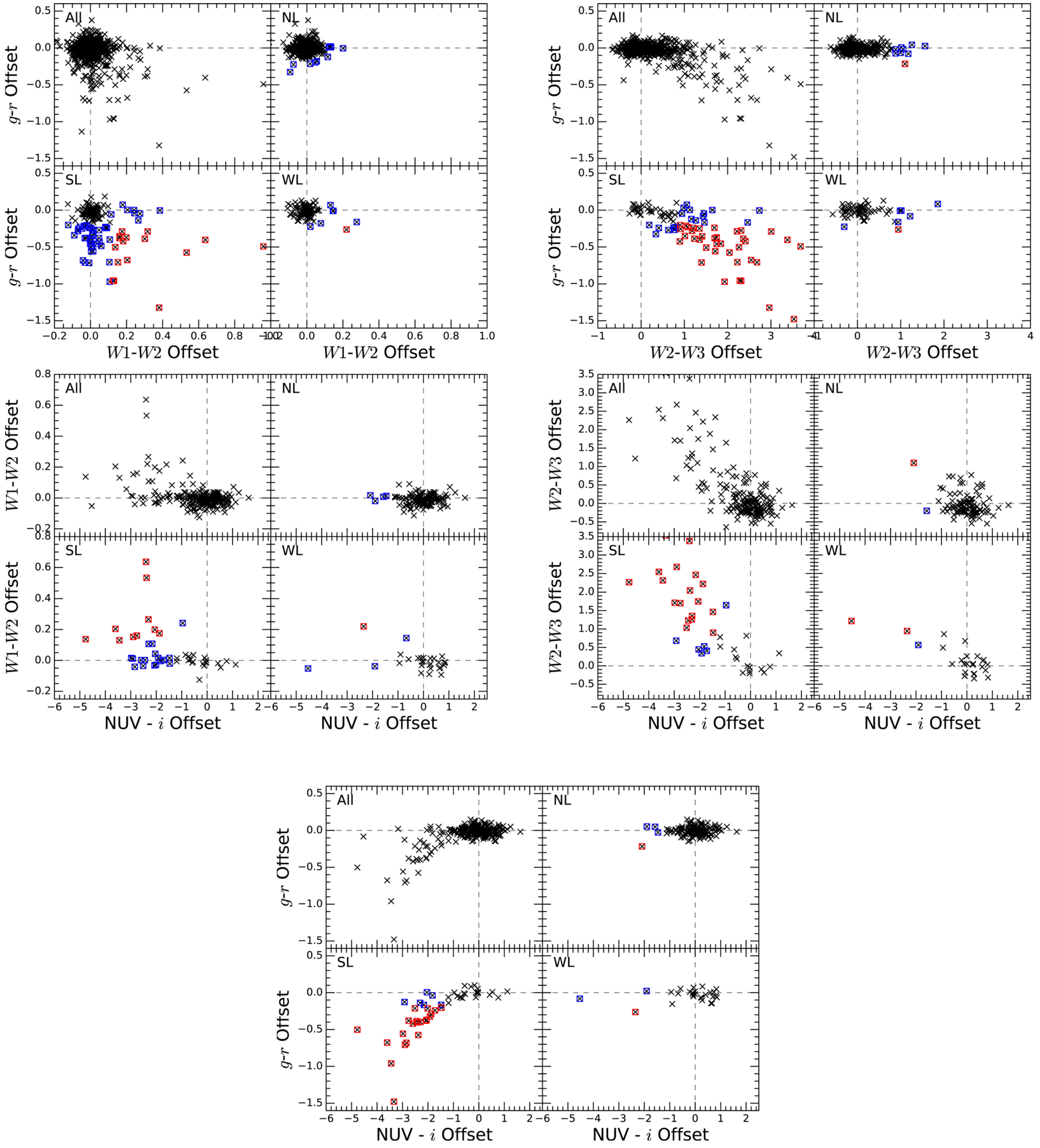

Figure 15. Plots of the various colour offsets against one another. The panels are split into: full sample (top left), non line emitters (top right), strong line emitters (bottom left) and weak line emitters (bottom right.) The blue squares indicate those BCGs with colour offsets in excess of $>2.5\sigma_p$ from zero in one colour and the red squares indicate those BCGs with significant colour offsets in both colours. Note that we only display sources with a S/N > 3, which limits the number of $W3$ and NUV detections.

et al. 2012; Green at al., in preparation) and hence is something to take into consideration when analysing activity in cluster cores.

The lack of non-line emitters, with significant offsets in multiple colours, supports our assumption that these are a fair representation of passively evolving galaxies. We believe that the few non-line emitters which are classed as active in our analysis are a result of scatter about a fixed cut-off value. The fraction of active non-line emitting BCGs can consequently provide a rough measure of the uncertainty in the active BCG fractions reported. The scatter about this colour cut-off can result from a number of sources, but primarily photometric uncertainty and contamination. A known source of contamination, in at least two of the BCGs in this sample, is from

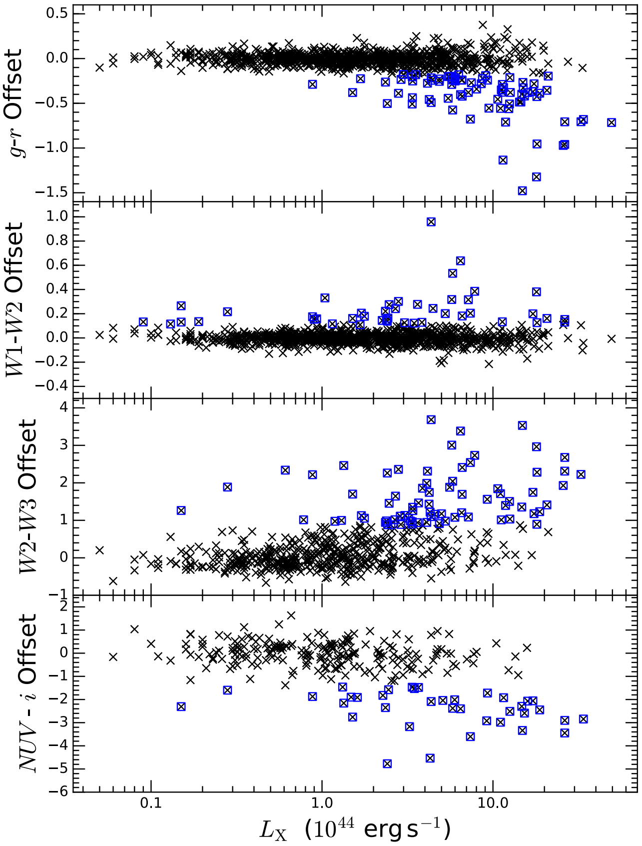

Figure 16. BCG colour offsets, against the X-ray luminosity of the host cluster, in the optical (top panel), mid-IR (second and third panels) and UV (bottom panel). We see that BCGs with colours which deviate from the quiescent BCG population tend to belong to more X-ray luminous clusters, consistent with BCG activity having a strong environmental dependence. Note that the first two panels are complete, but that the *W*3 and NUV detections are limited by S/N. So, since S/N is systematically lower at high redshift, high L_X clusters are preferentially excluded by selection effects.

lensed galaxies. There are clear gravitational arcs very close to the BCGs of A521 (Richard et al. 2010) and A2104 (Pierre et al. 1994). Both clusters have archival *Spitzer* observations, in which the arcs are clearly luminous in the mid-IR. Unfortunately the lower resolution of *WISE* means the emission of the BCGs and arcs are blended, probably accounting for the significant offset seen in the *W*2–*W*3 and *W*1–*W*2 for A521 and A2104, respectively. (Note: an excess of 24 µm emission was previously noted for the BCG of A521 in Hoffer et al. (2012), which is also likely a result of source blending of the arc). Given the rarity of gravitational arcs with low radius of curvature, this is unlikely to be a significant source of scatter. However, a few more may exist in such a large cluster sample.

3.5 BCG activity and cluster X-ray luminosity

The X-ray luminosity of a cluster is a combination of both the peaked emission of the core and the extended cluster emission. Hence it is reasonable to assume that, given the observed strong correlation between cool core clusters and BCG activity (see Introduction), any relationship seen between tracers of activity and L_X is indicative of this underlying link and suggestive that these clusters are also cool cores. In Fig. 16 we plot colour offsets against cluster L_X and find that BCGs with significant optical, mid-IR and UV colour offsets tend to belong to more X-ray luminous clusters. However, a high X-ray luminosity does not necessarily imply BCG activity. The number and proportion of BCGs with significant colour offsets, in bins of X-ray luminosity, are presented in Table 2, which confirms there is an apparent association between BCG activity and host cluster gas properties. This result agrees with the observations of O'Dea et al. (2008) who found BCG IR excesses preferentially in higher X-ray luminosity clusters.

Table 2. Number of BCGs with significant colour offsets, and optical emission lines, in bins of cluster X-ray luminosity. The results suggest active BCGs are preferentially found in high L_X clusters. Note the apparent decline in the weak line fraction in the highest L_X is likely a redshift dependence effect – specifically high L_X clusters are preferentially at high *z*, where the S/N in observations makes identifying weak lines difficult.

	Total 981	$L_X \geq 45$ 76	$L_X \geq 44$ 671	$42 < L_X < 44$ 310
g–*r*	79 (8 %)	35 (46 %)	78 (12 %)	1 (1 %)
*W*1–*W*2	45 (5 %)	8 (11 %)	36 (5 %)	9 (3 %)
*W*2–*W*3	75 (8 %)	19 (25 %)	70 (10 %)	5 (2 %)
NUV-*i*	37 (4 %)	12 (16 %)	34 (5 %)	3 (1 %)
Strong	144 (15 %)	34 (45 %)	127 (19 %)	17 (5 %)
Weak	100 (10 %)	2 (3 %)	61 (9 %)	39 (13 %)

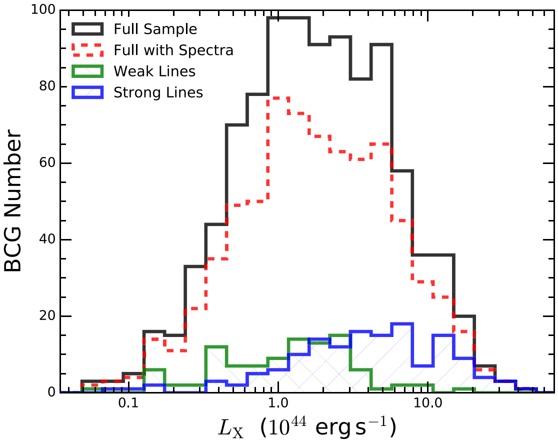

Figure 17. A histogram showing the host cluster X-ray luminosity distribution for the full sample of BCGs (solid black), the full sample of BCGs with spectroscopy (red dotted), as well as subsamples of BCGs with strong (blue hatch) and weak (green hatched) emission lines. We see that the presence of strong lines (hence BCG activity) is preferentially in the most X-ray luminous clusters.

The histograms in Fig. 17 show the X-ray distributions for clusters with line emitting BCGs and how this compares with the overall distribution. The presence of optical emission lines is strongly associated with the X-ray properties of the host clusters, with strong line emitters preferentially located in the more X-ray luminous clusters. From Table 2, we see that the fraction of BCGs which show signs of activity through the presence of strong lines increases with respect to X-ray luminosity. This positive trend is in agreement with the results of Samuele et al. (2011) who found fractions of 30 per cent, 18 per cent and 16 per cent for the Crawford et al. (1999) BCS sample of BCGs for the same L_X ranges, respectively. Note that the apparent deficit in weak line emitting BCGs at higher X-ray luminosities is likely to be an observational effect, in which high L_X clusters are more likely to be high redshift, where the detection of weak lines is more difficult.

Table 3. Same as Table 1, but for the 'X-ray luminosity complete' subsample of clusters with $L_X \geq 1 \times 10^{44}$ erg s^{-1} and $z \leq 0.2$.

	BCGs (No.)	Opt. (per cent)	MIR (per cent)	UV (per cent)	Combined (per cent)	Radio (per cent)
All	359	5	11	4	14	53
SL	61	23	31	16	43	90
WL	39	5	10	5	15	67
NL	177	0	5	1	6	42

Table 4. Same as Table 1, but for the subsample of clusters with $L_X \geq 1 \times 10^{44}$ erg s^{-1} and $z \leq 0.1$ to match the sample selection in Fraser-McKelvie et al. (2014).

	BCGs (No.)	Opt. (per cent)	MIR (per cent)	UV (per cent)	Combined (per cent)	Radio (per cent)
All	95	3	8	2	11	61
SL	17	18	29	6	35	88
WL	14	0	7	0	7	86
NL	52	0	0	2	2	48

The presence of emission lines in BCGs can be used as tracer of cool core clusters (Heckman 1981; Hu et al. 1985; Johnstone et al. 1987; Heckman et al. 1989; Crawford et al. 1999; McDonald 2011). So given we find a link between photometric colours and emission line status, we can then deduce that peculiar photometric colours also acts as a tracer of cool cores. This reinforces the assumptions given above that the peculiar colour and L_X association is reflective of the likely cool core status of these particular clusters.

The strong association between BCG activity and total X-ray luminosity of the host cluster, evident through the photometric excess and optical line emission, has important implications regarding cluster selection effects. Specifically, the fraction of active BCGs one discovers in any given cluster sample is dependent on the X-ray luminosity distribution of that sample. For example, S12 do not find any unusual coloured BCGs in g–r in the XCS sample, but this is not surprising given the low X-ray luminosity nature of that particular cluster sample. With this in mind we investigate the active BCG fraction for volume complete subsamples and make comparisons to the literature.

If we consider an 'X-ray luminosity complete' cluster subsample defined by $L_X \geq 1 \times 10^{44}$ erg s^{-1} and $z \leq 0.2$, (as indicated in Fig. 1), we find active BCG fractions as presented in Table 3, specifically that at least 14 per cent of clusters deviate from passivity in at least one colour. This is comparable to our overall figure of 14 per cent because the lower L_X and higher z sections of our full sample cancel out their relative effects.

Similarly, in Table 4 we summarize the BCG fractions within the subsample defined by $L_X \geq 1 \times 10^{44}$ erg s^{-1} and $z \leq 0.1$. This L_X–z distribution was chosen to match that of Fraser-McKelvie et al. (2014), who find 3 ± 1 per cent of their BCGs have a W2-W3 colour in excess of 1.5, suggestive that they are likely dominated by SF. We conversely find that >8 per cent of our BCGs in the same L_X–z space have a colour offset in *WISE*, increasing to at least 10 per cent if you include the optical and UV data. This disagreement we think reflects their use of raw *WISE* colours and of a simple colour cut to select star forming galaxies. In their plot a significant number of BCGs are offset from the bulk passive cloud in colour–colour space, yet do not satisfy the colour cut used. One would expect very few BCGs in the Universe to be forming stars on the level one would expect for a classically 'star forming' galaxy (like a spiral), but instead one should consider how a modest amount of star formation would make the *WISE* colours differ from the bulk passive cloud of BCGs in colour space.

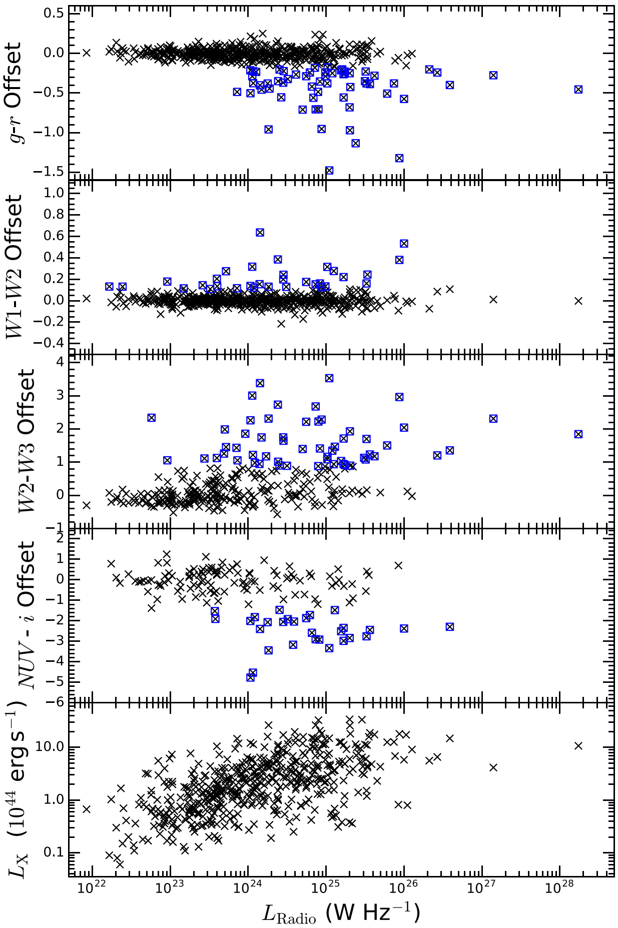

Figure 18. The 1.4 GHz radio luminosity of the BCGs against the optical, mid-IR and UV colour offsets (top four panels) and host cluster X-ray luminosity (bottom panel). The (blue) squares are indicative of offsets in excess of 2.5 σ_p.

An additional observational consideration for BCG activity is that the peaked X-ray emission in cool core clusters could be misinterpreted as a point source in shallow X-ray data. If the BCG of the cluster shows strong high ionization line emission, usually, and understandably, that X-ray source is identified as an AGN. But, the cluster may still be a significant contributor. This is best illustrated by the Phoenix cluster (McDonald et al. 2012), where the most X-ray luminous cluster was only identified because of the SPT SZ effect detection. Therefore caution is needed when interpreting the perceived rarity of BCGs hosting strong AGN as this identification bias could be masking systems such as H1821+644 (Russell et al. 2010) and 3C186 (Siemiginowska et al. 2010) where the cluster X-ray emission is a minority contributor to the total flux, but it would still be above the X-ray flux limit of a survey once the AGN contribution is removed.

3.6 Radio luminosity

We find 512 BCGs (52 per cent of total sample) have a 1.4 GHz radio detections within 45 arcsec in NVSS. In the colour offset against radio luminosity plots shown in Fig. 18 there appears to be a connection between the radio emission and colour offsets. The apparent trends in the top four panels are likely to be a reflection of the relation between X-ray luminosity and radio power (Hogan et al. 2015), shown in the bottom panel, rather than suggesting that the star formation is induced or triggered by the radio activity in the BCG. This does however support the idea of a feedback cycle between radiative cooling induced star formation and AGN activity. Whereby relic radio emission still exists from previous stages of AGN activity in these galaxies.

4 CONCLUSIONS

We investigated the PS1 optical, *WISE* mid-IR and *GALEX* UV photometry for Brightest Cluster Galaxies in 981 *ROSAT* All Sky Survey X-ray selected clusters. The sample consists of clusters in the redshift range, $0.03 < z < 0.5$ with an X-ray luminosity range of 5×10^{43} erg s^{-1} $< L_X < 5 \times 10^{45}$ erg s^{-1}. The principal aim was to search for signs of star formation and/or AGN activity in BCGs by looking for photometric colours which deviate from that expected for a passive BCG. The main results are summarized as follows.

(i) At least 14 per cent of the BCGs in our full sample show a significant colour deviation from passivity in at least one colour. In the optical we find 8 per cent are significantly blue in *PS*1 *g*–*r*. In the mid-IR we find at least 9 per cent show a significant colour offset in either W1–W2 or W2–W3, with 5 per cent showing enhanced *W*2 emission, and at least 8 per cent showing enhanced *W*3 emission. In the NUV we find at least 4 per cent of BCGs show an enhanced NUV emission, shown as a significant NUV-*i* colour offset. We stress that due to incompleteness these fractions represent lower limits for the NUV and *W*3. We interpret these colour deviations as a result of star formation and/or AGN activity within the BCG. Details regarding each of these active BCG candidates are provided in Table A1.

(ii) We find that across all wavelengths the presence of optical emission lines and atypical photometric colours are strongly associated. This reinforces our interpretation of these BCGs being ‘active’. We find that the majority of BCGs are non-line emitting and do not exhibit signs of enhanced emission, consistent with passivity.

(iii) We find that BCG activity has a strong association with the host cluster X-ray luminosity. Specifically, the fraction of peculiarly coloured BCGs is much higher in high $L_{\rm X}$ clusters. This has important implications for the apparent prevalence of active BCGs and the selection function of a cluster sample. Additionally, there is an active identification bias against BCGs which host AGN being included in a cluster sample given the presumption that the AGN will be the majority contributor to the X-ray emission, when in fact the cluster emission alone may be still be sufficient to reach the selection flux limit.

(iv) We find that significant colour offsets in one wavelength regime is often associated with a significant offset in another, but not always. In the former case this illustrates the common origin of these colours at different wavelengths, but in the latter shows the benefit of a multiwavelength analysis, in which we can trace activity over complimentary time-scales and degrees of obscuration.

(v) We find that the BCG luminosity, in both the *i* and *W*1 bands, correlates with the X-ray luminosity of the host cluster. Specifically the most luminous, and hence most massive, BCGs tend to reside in the more X-ray luminous, and hence massive, clusters.

(vi) The optical colours of the cluster red sequence are remarkably tightly constrained given the range in $L_{\rm X}$, indicative of the homogeneity in cluster galaxies across mass and redshift. For the majority of BCGs, this is also the case. So where BCGs are passively evolving, they do so in a similar fashion to one another.

(vii) We have shown we are able to measure photometric excesses in active BCGs up to at least $z = 0.5$, with potential to go to higher redshift. Hence, the same analysis could be applied to future, larger cluster samples. This creates opportunity with the new generation of X-ray telescopes, such as eROSITA, due to make observations in the near future, which will fill in the $L_{\rm X}$–z parameter space. Combined with large photometric surveys such as the LSST one could identify a large number of ‘active’ BCG candidates, which would be vital in really constraining the prevalence of activity in BCGs and better understanding the role of feedback in these systems.

ACKNOWLEDGEMENTS

We thank the anonymous referee for their contribution in improving this manuscript. TSG received financial support from the Science and Technology Facilities Council (STFC) grant ST/K501979/1. ACE acknowledges support from STFC grant ST/I001573/1. JPS gratefully acknowledges a Hintze Research Fellowship.

The Pan-STARRS1 Surveys (PS1) have been made possible through contributions by the Institute for Astronomy, the University of Hawaii, the Pan-STARRS Project Office, the Max-Planck Society and its participating institutes, the Max Planck Institute for Astronomy, Heidelberg and the Max Planck Institute for Extraterrestrial Physics, Garching, The Johns Hopkins University, Durham University, the University of Edinburgh, the Queen’s University Belfast, the Harvard-Smithsonian Center for Astrophysics, the Las Cumbres Observatory Global Telescope Network Incorporated, the National Central University of Taiwan, the Space Telescope Science Institute, and the National Aeronautics and Space Administration under Grant No. NNX08AR22G issued through the Planetary Science Division of the NASA Science Mission Directorate, the National Science Foundation Grant No. AST-1238877, the University of Maryland, Eotvos Lorand University (ELTE), and the Los Alamos National Laboratory.

All WISE makes use of data from *WISE*, which is a joint project of the University of California, Los Angeles, and the Jet Propulsion Laboratory/California Institute of Technology, and NEOWISE, which is a project of the Jet Propulsion Laboratory/California Institute of Technology. *WISE* and NEOWISE are funded by the National Aeronautics and Space Administration.

This research has made use of the NASA/IPAC Extragalactic Database (NED) which is operated by the Jet Propulsion Laboratory, California Institute of Technology, under contract with the National Aeronautics and Space Administration.

REFERENCES

Andreon S., 2003, A&A, 409, 37
Assef R. J. et al., 2013, ApJ, 772, 26
Bertin E., Arnouts S., 1996, A&AS, 117, 393
Best P., von der Linden A., Kauffmann G., Heckman T., Kaiser C., 2007, MNRAS, 379, 894
Boehringer H., Voges W., Fabian A. C., Edge A. C., Neumann D. M., 1993, MNRAS, 264, L25
Böhringer H. et al., 2000, ApJS, 129, 435
Böhringer H. et al., 2004, A&A, 425, 367
Bruzual G., Charlot S., 2003, MNRAS, 344, 1000
Burns J. O., 1990, AJ, 99, 14
Burns J. O., Gregory S. A., Holman G. D., 1981, ApJ, 250, 450
Cardelli J. A., Clayton G. C., Mathis J. S., 1989, ApJ, 345, 245
Cardiel N., Gorgas J., Aragon-Salamanca A., 1998, MNRAS, 298, 977

Cavagnolo K. W., Donahue M., Voit G. M., Sun M., 2008, ApJ, 683, L107
Condon J. J., Cotton W. D., Greisen E. W., Yin Q. F., Perley R. A., Taylor G. B., Broderick J. J., 1998, AJ, 115, 1693
Crawford C. S., Allen S. W., Ebeling H., Edge A. C., Fabian A. C., 1999, MNRAS, 306, 857
Dickey J. M., Lockman F. J., 1990, ARA&A, 28, 215
Donahue M. et al., 2010, ApJ, 715, 881
Donahue M., de Messières G. E., O'Connell R. W., Voit G. M., Hoffer A., McNamara B. R., Nulsen P. E. J., 2011, ApJ, 732, 40
Dunn R. J. H., Fabian A. C., 2006, MNRAS, 373, 959
Ebeling H., Edge A. C., Bohringer H., Allen S. W., Crawford C. S., Fabian A. C., Voges W., Huchra J. P., 1998, MNRAS, 301, 881
Ebeling H., Edge A. C., Allen S. W., Crawford C. S., Fabian A. C., Huchra J. P., 2000, MNRAS, 318, 333
Ebeling H., Edge A. C., Henry J. P., 2001, ApJ, 553, 668
Ebeling H., Barrett E., Donovan D., Ma C.-J., Edge A. C., van Speybroeck L., 2007, ApJ, 661, L33
Ebeling H., Edge A. C., Mantz A., Barrett E., Henry J. P., Ma C. J., van Speybroeck L., 2010, MNRAS, 407, 83
Edge A. C., 1991, MNRAS, 250, 103
Edge A. C., 2001, MNRAS, 328, 762
Edge A. C., Ivison R. J., Smail I., Blain A. W., Kneib J.-P., 1999, MNRAS, 306, 599
Edge A. C., Wilman R. J., Johnstone R. M., Crawford C. S., Fabian A. C., Allen S. W., 2002, MNRAS, 337, 49
Edge A. C. et al., 2010, A&A, 518, L46
Egami E. et al., 2006a, ApJ, 647, 922
Egami E., Rieke G. H., Fadda D., Hines D. C., 2006b, ApJ, 652, L21
Fabian A., 1994, ARA&A, 32, 277
Fabian A. C., 2012, ARA&A, 50, 455
Fabian A. C., Sanders J. S., Williams R. J. R., Lazarian A., Ferland G. J., Johnstone R. M., 2011, MNRAS, 417, 172
Ferland G. J., Fabian A. C., Hatch N. A., Johnstone R. M., Porter R. L., van Hoof P. A. M., Williams R. J. R., 2009, MNRAS, 392, 1475
Fogarty K., Postman M., Connor T., Donahue M., Moustakas J., 2015, ApJ, 813, 117
Fraser-McKelvie A., Brown M. J. I., Pimbblet K. A., 2014, MNRAS, 444, L63
Hamer S. L., Edge A. C., Swinbank A. M., Wilman R. J., Russell H. R., Fabian A. C., Sanders J. S., Salomé P., 2012, MNRAS, 421, 3409
Hamer S. L. et al., 2016, MNRAS, 460, 1758
Heckman T. M., 1981, ApJ, 250, L59
Heckman T. M., Baum S. A., van Breugel W. J. M., McCarthy P., 1989, ApJ, 338, 48
Hicks A. K., Mushotzky R., Donahue M., 2010, ApJ, 719, 1844
Hlavacek-Larrondo J., Fabian A. C., Edge A. C., Ebeling H., Sanders J. S., Hogan M. T., Taylor G. B., 2012, MNRAS, 421, 1360
Hlavacek-Larrondo J., Fabian A. C., Edge A. C., Ebeling H., Allen S. W., Sanders J. S., Taylor G. B., 2013, MNRAS, 431, 1638
Hlavacek-Larrondo J. et al., 2015, ApJ, 805, 35
Hoffer A. S., Donahue M., Hicks A., Barthelemy R. S., 2012, ApJS, 199, 23
Hogan M. T. et al., 2015, MNRAS, 453, 1201
Hu E. M., Cowie L. L., Wang Z., 1985, ApJS, 59, 447
Isobe T., Feigelson E. D., Akritas M. G., Babu G. J., 1990, ApJ, 364, 104
Johnstone R. M., Fabian A. C., Nulsen P. E. J., 1987, MNRAS, 224, 75
Jones D. H. et al., 2004, MNRAS, 355, 747
Kron R. G., 1980, ApJS, 43, 305
Lauer T. R., Postman M., Strauss M. A., Graves G. J., Chisari N. E., 2014, ApJ, 797, 82
Lidman C. et al., 2012, MNRAS, 427, 550
Lin Y.-T., Mohr J. J., 2004, ApJ, 617, 879
Lin Y.-T., Mohr J. J., Stanford S. A., 2003, ApJ, 591, 749
Liu F. S., Mao S., Meng X. M., 2012, MNRAS, 423, 422
McDonald M., 2011, ApJ, 742, L35
McDonald M. et al., 2012, Nature, 488, 349
McNamara B. R., Nulsen P. E. J., 2007, ARA&A, 45, 117
McNamara B. R., Nulsen P. E. J., 2012, New J. Phys., 14, 055023
McNamara B. R. et al., 2000, ApJ, 534, L135
Martel H., Robichaud F., Barai P., 2014, ApJ, 786, 79
Martin D. C. et al., 2005, ApJ, 619, L1
Mehrtens N. et al., 2012, MNRAS, 423, 1024
Mei S. et al., 2006, ApJ, 644, 759
Mittal R. et al., 2012, MNRAS, 426, 2957
O'Dea C. P. et al., 2008, ApJ, 681, 1035
Pierre M., Soucail G., Boehringer H., Sauvageot J. L., 1994, A&A, 289, L37
Quillen A. C. et al., 2008, ApJS, 176, 39
Rafferty D. A., McNamara B. R., Nulsen P. E. J., Wise M. W., 2006, ApJ, 652, 216
Rafferty D. A., McNamara B. R., Nulsen P. E. J., 2008, ApJ, 687, 899
Rawle T. D. et al., 2012, ApJ, 747, 29
Richard J. et al., 2010, MNRAS, 404, 325
Romer A. K., Viana P. T. P., Liddle A. R., Mann R. G., 2001, ApJ, 547, 594
Russell H. R., Fabian A. C., Sanders J. S., Johnstone R. M., Blundell K. M., Brandt W. N., Crawford C. S., 2010, MNRAS, 402, 1561
Russell H. R., McNamara B. R., Edge A. C., Hogan M. T., Main R. A., Vantyghem A. N., 2013, MNRAS, 432, 530
Salomé P., Combes F., 2003, A&A, 412, 657
Samuele R., McNamara B. R., Vikhlinin A., Mullis C. R., 2011, ApJ, 731, 31
Sanderson A. J. R., Edge A. C., Smith G. P., 2009, MNRAS, 398, 1698
Schlafly E. F., Finkbeiner D. P., 2011, ApJ, 737, 103
Siemiginowska A., Burke D. J., Aldcroft T. L., Worrall D. M., Allen S., Bechtold J., Clarke T., Cheung C. C., 2010, ApJ, 722, 102
Smith G. P. et al., 2010, MNRAS, 409, 169
Stanford S., Eisenhardt P., Dickinson M., 1998, ApJ, 492, 461
Stanford S. A., Gonzalez A. H., Brodwin M., Gettings D. P., Eisenhardt P. R. M., Stern D., Wylezalek D., 2014, ApJS, 213, 25
Stott J. P., Edge A. C., Smith G. P., Swinbank A. M., Ebeling H., 2008, MNRAS, 384, 1502
Stott J. P. et al., 2010, ApJ, 718, 23
Stott J. P. et al., 2012, MNRAS, 422, 2213 (S12)
Thomas D., Maraston C., Bender R., Mendes de Oliveira C., 2005, ApJ, 621, 673
Tonry J. L. et al., 2012, ApJ, 750, 99
Valentijn E. A., Bijleveld W., 1983, A&A, 125, 223
van Dokkum P. G., van der Marel R. P., 2007, ApJ, 655, 30
Voges W. et al., 1999, A&A, 349, 389
Wang J., Overzier R., Kauffmann G., von der Linden A., Kong X., 2010, MNRAS, 401, 433
Whiley I. M. et al., 2008, MNRAS, 387, 1253
White D. A., Jones C., Forman W., 1997, MNRAS, 292, 419
Wright E. L. et al., 2010, AJ, 140, 1868
York D. G. et al., 2000, AJ, 120, 1579

APPENDIX A: TABLE OF 'ACTIVE' BCG CANDIDATES

Table A1. A table of those BCGs measured to be significantly offset in one colour or more (i.e. a colour offset in excess of $2.5\sigma_p$). The table key is as follows: (0) Cluster X-ray luminosity, in 0.1–2.4 keV band, in units of $10^{44}\,\mathrm{erg\,s^{-1}}$, (1) indicates whether the BCG has strong (S), weak (W) or no (N) optical emission lines or if no spectra available (–) (2) a PS1 g–r colour offset <-0.18 mag, (3) a *WISE* $W1$–$W2$ offset >0.11 mag, (4) a *WISE* $W2$–$W3$ colour offset >0.87 mag and (5) a *GALEX* NUV-i colour offset <-1.43 mag. (a) The symbols in these columns are as follows: if a number is present this is the colour offset value and indicates a significant deviation from passivity, '×' indicates a lack of a significant offset, '–' indicates this BCG not observed, and '..' indicates a poor S/N.

Cluster ID	BCG R.A. (J2000)	BCG DEC (J2000)	Redshift	L_X (0)	Lines (1)	g–r (2a)	$W1$–$W2$ (3a)	$W2$–$W3$ (4a)	NUV-i (5a)
RXJ0008.0-1151	00:07:57.0	−11:51:44	0.21	1.48	N	×	×	..	−1.90
RXJ0010.9+2909	00:10:53.4	+29:09:39	0.33	4.29	W	×	×	1.21	−4.53
A11	00:12:33.8	−16:28:07	0.15	0.88	S	−0.29	0.18	2.22	−1.87
A22	00:20:43.1	−25:42:28	0.14	3.46	N	×	0.12	..	–
MACSJ0025.4-1222	00:25:33.0	−12:23:16	0.48	11.45	–	−1.13	×	..	–
RXJ0045.9-1723	00:45:54.8	−17:23:29	0.06	0.15	W	×	0.13	×	–
S84	00:49:22.8	−29:31:12	0.11	1.77	S	×	0.18	1.06	..
Z348	01:06:49.4	+01:03:22	0.25	7.38	S	−0.68	0.20	2.54	−3.60
A145	01:06:53.3	−02:28:56	0.19	1.30	N	×	×	1.00	–
MACSJ0111.5+0855	01:11:31.5	+08:55:41	0.48	15.04	N	−0.33	×	..	–
MACSJ0150.3-1005	01:50:21.3	−10:05:30	0.36	6.61	S	−0.42	0.18	2.40	–
MACSJ0159.8-0849	01:59:49.3	−08:49:58	0.40	18.06	S	−0.43	×	0.89	–
A291	02:01:43.1	−02:11:48	0.20	5.97	S	−0.21	×	..	−2.01
A368	02:37:27.7	−26:30:28	0.22	4.23	S	×	×	1.43	–
RXJ0238.8-1258	02:38:49.3	−12:58:49	0.20	2.53	N	×	×	0.88	×
MACSJ0242.5-2132	02:42:35.9	−21:32:25	0.31	14.74	S	−0.40	×	1.35	−2.30
A383	02:48:03.3	−03:31:44	0.19	5.09	S	×	×	×	−2.04
A3088	03:07:02.2	−28:39:56	0.25	7.48	S	−0.27	×	×	–
MACSJ0326.8-0043	03:26:49.9	−00:43:51	0.45	14.29	S	−0.49	×	..	–
MACSJ0329.6-0211	03:29:41.6	−02:11:46	0.45	11.85	S	−0.71	×	1.39	–
RXJ0331.1-2100	03:31:05.9	−21:00:32	0.19	5.48	S	−0.20	×	×	–
RXJ0353.0+1941	03:52:59.0	+19:40:59	0.11	2.47	S	×	0.28	1.46	–
MACSJ0404.6+1109	04:04:33.7	+11:07:53	0.36	11.35	–	−0.29	0.14	..	–
A483	04:15:57.6	−11:32:53	0.28	5.27	–	×	×	0.97	–
MACSJ0417.5-1154	04:17:34.7	−11:54:32	0.44	33.83	S	−0.68	×	..	−2.84
MACSJ0429.6-0253	04:29:36.0	−02:53:06	0.40	12.64	S	−0.38	×	..	–
RXJ0437.1+0043	04:37:09.6	+00:43:51	0.28	8.68	N	−0.22	×	..	–
RXJ0439.0+0520	04:39:02.3	+05:20:42	0.21	5.83	S	−0.24	×	×	–
RXJ0448.2+0952	04:48:12.8	+09:53:01	0.15	2.90	–	−0.23	×	..	–
A521	04:54:06.9	−10:13:24	0.25	9.26	N	×	×	1.56	–
RXJ0505.2-0217	05:05:16.7	−02:19:24	0.23	3.05	–	×	×	1.13	–
RXJ0524.3+0329	05:24:19.1	+03:29:54	0.15	2.43	–	×	0.16	..	–
RXJ0611.0-2735	06:11:01.2	−27:35:33	0.04	0.15	S	×	0.27	1.27	−2.31
Z1121	06:31:22.7	+25:01:06	0.08	2.38	W	–	0.15	0.99	–
CIZAJ0640.1-1253	06:40:07.2	−12:53:14	0.14	7.18	–	−0.38	0.32	1.09	–
CIZAJ0710.4+2240	07:10:23.8	+22:40:02	0.29	11.30	–	−0.35	×	..	..
CIZAJ0719.5+0043	07:19:36.0	+00:42:33	0.22	9.05	–	−0.19	×	..	–
PKS745-191	07:47:31.4	−19:17:39	0.10	12.50	S	−0.51	×	1.50	–
RXJ0815.5-0308	08:15:27.8	−03:08:27	0.20	5.58	–	−0.20	×	..	–
RXJ0821.0+0751	08:21:02.3	+07:51:47	0.11	1.34	S	×	×	2.46	−2.16
RXJ0834.9+5534	08:34:55.0	+55:34:20	0.24	4.14	S	−0.28	×	2.31	×
Z1883	08:42:55.9	+29:27:26	0.19	3.37	S	−0.20	×	0.90	−1.47
Z2089	09:00:37.0	+20:53:40	0.23	6.46	S	−0.40	0.64	3.38	−2.40
MACSJ0913.7+4056	09:13:45.6	+40:56:27	0.44	14.87	S	−1.48	1.77	3.52	−3.34
Hyd-A	09:18:05.7	−12:05:43	0.05	6.56	S	−0.24	×	1.21	–
A854	09:42:01.1	+08:58:19	0.21	3.40	N	×	×	1.26	–
RBS797	09:47:12.7	+76:23:13	0.34	20.69	S	−0.36	0.16	1.41	−2.88
RXJ1000.4+4409	10:00:31.0	+44:08:43	0.15	2.25	W	×	0.14	..	×
A910	10:03:00.2	+67:07:56	0.21	3.47	–	×	×	×	−1.53
A926	10:06:40.2	+21:40:14	0.18	1.70	S	×	0.20	1.12	–
MS1006.0+1202	10:08:47.7	+11:47:38	0.26	3.87	W	×	×	1.85	–
Z3146	10:23:39.6	+04:11:10	0.29	26.29	S	−0.96	0.13	2.31	−3.45
A3444	10:23:50.2	−27:15:23	0.25	15.96	S	−0.38	×	×	−2.07
A1068	10:40:44.4	+39:57:11	0.14	5.74	S	−0.29	0.32	3.01	–
A1084	10:44:32.9	−07:04:07	0.13	4.10	S	×	×	0.95	×

Table A1 – *continued*

Cluster ID	BCG R.A. (J2000)	BCG DEC (J2000)	Redshift	L_X (0)	Lines (1)	g–r (2a)	$W1$–$W2$ (3a)	$W2$–$W3$ (4a)	NUV-i (5a)
A1126	10:53:50.2	+16:51:02	0.09	1.19	–	×	×	0.98	×
A1211	11:14:50.3	−12:13:50	0.19	3.21	N	×	×	1.05	×
Z3959	11:15:51.8	+01:29:54	0.35	15.29	S	−0.42	×	..	−2.59
RXJ1124.5+4351	11:24:29.7	+43:51:25	0.37	8.02	S	−0.34	×	..	–
RXJ1128.1+7529	11:28:09.9	+75:29:35	0.17	0.93	–	×	0.16	..	–
MACSJ1141.6-1905	11:41:40.8	−19:05:15	0.30	3.84	–	×	0.13	..	–
A1451	12:03:16.8	−21:32:55	0.20	5.00	N	×	×	1.17	–
MACSJ1218.4+4012	12:18:28.6	+40:12:38	0.30	5.75	–	−0.20	×	..	–
RXJ1259.1+4129	12:59:08.6	+41:29:37	0.28	2.99	W	−0.18	×	..	–
RXJ1301.0-2312	13:00:58.5	−23:12:15	0.13	1.51	S	−0.38	0.16	1.70	−2.76
A1664	13:03:42.6	−24:14:42	0.13	4.24	S	−0.46	×	1.75	−3.12
A1704[a]	13:14:24.6	+64:34:31	0.22	4.35	N	−0.22	×	1.10	−2.09
A1750b	13:31:11.0	−01:43:38	0.08	0.61	–	×	×	2.34	×
RXJ1336.0-0331	13:35:60.0	−03:31:28	0.17	1.61	W	×	×	×	−1.91
MACSJ1347.5-1144	13:47:30.7	−11:45:09	0.45	49.41	S	−0.72	×	..	–
A1795	13:48:52.5	+26:35:34	0.06	9.19	S	×	×	×	−2.92
RBS1322	13:50:22.1	+09:40:10	0.13	3.67	S	×	×	1.46	−1.48
MACSJ1354.6+7715	13:54:43.0	+77:15:16	0.40	6.60	S	−0.24	×	1.69	–
RXJ1359.3+7447	13:59:16.9	+74:46:42	0.20	1.68	W	−0.23	×	×	–
RXJ1359.9+1414	13:59:57.3	+14:14:17	0.21	2.67	W	×	×	1.01	..
A1835	14:01:02.2	+02:52:42	0.25	26.31	S	−0.71	0.15	2.67	−2.90
RXJ1401.3+2501	14:01:17.8	+25:01:50	0.41	6.30	–	−0.18	×	..	–
MACSJ1411.3+5212	14:11:20.4	+52:12:09	0.46	10.67	S	−0.45	×	1.84	–
A1910	14:24:24.4	+25:14:28	0.23	2.41	S	−0.50	0.14	2.26	−4.77
A1918	14:25:22.5	+63:11:53	0.14	2.45	N	×	×	×	−1.58
RXJ1427.2+4407	14:27:16.1	+44:07:30	0.49	17.39	S	−0.28	×	1.17	–
RXJ1434.7+1721	14:34:42.9	+17:21:57	0.04	0.09	N	×	0.13	×	–
RXJ1447.4+0827	14:47:26.0	+08:28:25	0.38	25.77	S	−0.97	0.11	1.92	–
Z7160	14:57:15.1	+22:20:34	0.26	11.54	S	−0.32	×	×	−1.92
RXJ1459.1-0842	14:59:05.2	−08:42:36	0.10	1.15	N	×	0.12	×	–
S780	14:59:28.8	−18:10:45	0.24	11.07	S	−0.56	×	1.71	−2.98
RXJ1504.1-0248	15:04:07.5	−02:48:16	0.22	32.73	S	−0.71	×	2.22	−4.72
RXJ1512.8-0127	15:12:52.6	−01:28:26	0.12	0.78	N	×	×	1.01	–
A2055	15:18:45.7	+06:13:56	0.10	3.62	W	×	0.28	0.94	–
MACSJ1532.8+3021	15:32:53.8	+30:20:59	0.34	18.10	S	−0.95	0.13	2.28	–
A2104	15:40:07.9	−03:18:15	0.15	5.26	N	×	0.20	×	–
MACSJ1551.9-0207	15:51:58.6	−02:07:50	0.30	5.47	–	−0.44	×	..	–
A2146	15:56:14.2	+66:20:52	0.23	7.82	S	×	0.38	2.73	..
PKS1555-140	15:58:21.9	−14:09:58	0.10	4.57	S	×	×	1.16	–
RXJ1600.0-0354	16:00:02.5	−03:54:35	0.27	4.39	–	−0.24	×	..	–
A2147b	16:03:38.1	+15:54:02	0.11	2.69	S	×	0.24	1.65	×
RXJ1614.3+5442	16:14:15.4	+54:43:28	0.33	3.53	N	−0.18	×	..	–
MACSJ1621.3+3810	16:21:24.7	+38:10:08	0.47	12.38	S	−0.56	×	..	–
A2204	16:32:47.0	+05:34:31	0.15	14.97	S	−0.27	×	×	–
RBS1634	17:17:07.0	+29:31:21	0.28	14.57	S	−0.49	×	..	–
Z8193	17:17:19.2	+42:26:57	0.18	3.39	S	−0.25	×	1.35	–
Z8197	17:18:11.9	+56:39:56	0.11	2.27	S	×	×	×	−1.82
RXJ1720.2+2637	17:20:10.1	+26:37:32	0.16	9.29	S	−0.24	×	×	−1.72
A2262	17:23:21.6	+23:50:39	0.23	4.10	–	×	×	1.98	–
A2270	17:27:23.5	+55:10:53	0.24	2.80	S	−0.39	0.30	2.36	–
Z8276	17:44:14.5	+32:59:29	0.08	3.29	S	×	×	0.98	–
CIZAJ1804.1+0042	18:04:08.9	+00:42:22	0.09	2.89	–	×	×	0.89	–
RXJ1817.8+6824	18:17:44.5	+68:24:25	0.29	3.38	–	−0.44	×	×	–
RGBJ1832+688	18:32:35.8	+68:48:05	0.20	4.86	S	−0.25	×	0.91	..
CIZAJ1904.2+3627	19:04:11.9	+36:26:59	0.08	0.90	–	×	0.16	×	–
CIZAJ1917.6-1315	19:17:36.2	−13:15:11	0.18	3.25	–	×	×	..	−3.17
MACSJ1931.8-2634	19:31:49.7	−26:34:32	0.35	17.98	S	−1.32	0.38	2.96	–
Cyg-A	19:59:28.3	+40:44:02	0.06	4.35	S	−0.49	0.96	3.69	–
MRC2011-246	20:14:51.8	−24:30:23	0.16	12.56	S	−0.21	×	1.03	−2.51

Table A1 – *continued*

Cluster ID	BCG R.A. (J2000)	BCG DEC (J2000)	Redshift	L_X (0)	Lines (1)	g–r (2a)	$W1$–$W2$ (3a)	$W2$–$W3$ (4a)	NUV-i (5a)
RXJ2020.3-2225	20:20:22.6	−22:25:32	0.29	5.58	–	×	×	1.88	–
RXJ2043.2-2144	20:43:14.6	−21:44:34	0.20	4.46	S	×	0.24	..	–
RXJ2100.0-2426	20:59:55.6	−24:25:45	0.08	0.28	–	×	0.22	1.89	−1.60
RXJ2125.4+1742	21:25:22.0	+17:43:05	0.22	3.37	–	−0.51	×	0.96	–
MACSJ2134.6-2706	21:34:36.0	−27:05:55	0.36	6.01	–	−0.25	×	..	–
RGBJ2138+359	21:38:21.1	+35:58:23	0.11	1.04	–	×	0.33	×	–
MS2137.3-2353	21:40:15.2	−23:39:40	0.31	11.36	S	−0.38	×	..	–
MACSJ2149.3+0951	21:49:19.6	+09:51:37	0.38	8.55	–	−0.28	×	..	–
A2390	21:53:37.0	+17:41:42	0.23	18.77	S	−0.39	×	1.23	−2.45
RXJ2213.1-2754	22:13:05.9	−27:54:20	0.03	0.13	S	×	0.12	×	–
A2442	22:25:51.2	−06:35:34	0.09	1.32	N	×	×	..	−1.46
MACSJ2229.7-2755	22:29:45.2	−27:55:35	0.32	11.19	S	−0.35	×	1.01	–
MACSJ2243.3-0935	22:43:20.7	−09:35:18	0.45	21.05	N	−0.20	×	..	–
CIZAJ2302.6+7136	23:02:38.6	+71:36:25	0.14	2.87	–	×	×	1.11	–
RXJ2311.3-0946	23:11:18.9	−09:46:22	0.49	9.47	S	−0.55	×	..	–
RXJ2320.9-0433	23:20:54.2	−04:34:02	0.19	2.42	N	×	×	0.88	–
A2597	23:25:19.7	−12:07:26	0.09	5.99	S	−0.23	×	1.08	..
RXJ2326.3-2406	23:26:14.2	−24:06:30	0.06	0.19	N	×	0.14	..	–
A2627	23:36:42.1	+23:55:29	0.12	2.35	W	−0.26	0.22	0.94	−2.35
PKS2338+000	23:41:07.0	+00:18:33	0.28	5.81	S	−0.58	0.53	2.04	−2.38
A2667	23:51:39.4	−26:05:02	0.23	17.13	S	−0.37	0.20	1.74	−2.06
RXJ2355.4-1027	23:55:25.6	−10:27:22	0.29	3.04	N	×	0.13	..	–

[a] The BCG of A1704 has an SDSS spectra on its core, which shows no emission lines. But in the imaging there is clearly an optically blue component within the BCG and just North of its core, which does not have spectroscopy. We detect this in our photometry and suspect this is associated with activity in the BCG, but projection cannot be ruled out.

This paper has been typeset from a TEX/LATEX file prepared by the author.